

Graph skeletonization of high-dimensional point cloud data via topological method*

Lucas Magee

Department of Computer Science and Engineering
University of California, San Diego
La Jolla, CA 92122
lmagee@ucsd.edu

Yusu Wang

Halcioğlu Data Science Institute
University of California, San Diego
La Jolla, CA, USA
yusuwang@ucsd.edu

September 29, 2021

Abstract

Geometric graphs form an important family of hidden structures behind data. In this paper, we develop an efficient and robust algorithm to infer a graph skeleton behind a point cloud dataset (PCD) embedded in high-dimensional space. Previously, there has been much work to recover a hidden graph from a low-dimensional density field, or from a relatively clean high-dimensional PCD (in the sense that the input points are within a small bounded distance to a true hidden graph). Our proposed approach builds upon the recent line of work on using a persistence-guided discrete Morse (DM) theory based approach to reconstruct a geometric graph from a density field defined over a triangulation of low-dimensional Euclidean domain. In particular, we first give a very simple generalization of this DM-based algorithm from a density-function perspective to a general filtration perspective. On the theoretical front, we show that the output of the generalized algorithm contains a so-called lexicographic-optimal persistent cycle basis w.r.t the input filtration, justifying that the output is indeed meaningful. On the algorithmic front, this generalization allows us to use the idea of sparsified weighted Rips filtration (developed by Buchet et al) to develop a new graph reconstruction algorithm for noisy point cloud data (PCD) (which do not need to be embedded). The new algorithm is robust to background noise and non-uniform distribution of input points. We provide various experimental results to show the efficiency and effectiveness of our new graph reconstruction algorithm for PCDs.

1 Introduction

Modern complex data, or the space where data is sampled from, often has an underlying simpler and potentially non-linear, structure. A key step in modern data analysis is to model and extract such hidden structures. A particularly interesting type of non-linear structure is a (geometric) graph structure, which can be thought of as a 1-D *singular manifold*, consisting of pieces of 1-manifolds (curves) glued together. Graph structures are common in practice, such as river networks and dark matter filament structures in cosmology. Graphs can also be natural models for the evolution of trends behind data (e.g, the evolution of topics in twitter data). While there have been beautiful lines of work on manifold learning [35, 37, 4, 19], recovering singular manifolds is

*This work is partially supported by National Science Foundation (NSF) under grants RI-1815697 and OAC-2107076, and by National Institutes of Health (NIH) under grant RF1MH125317.

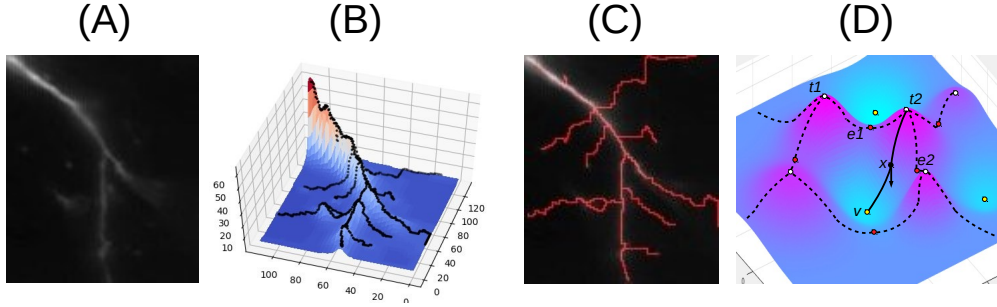


Figure 1: A practical example of DM graph reconstruction. (A) The image (downloaded from www.brainimagelibrary.org/) contains neuronal branches that we aim to reconstruct. (B) View the image as a density function, we show the graph of this function, and mountain ridges of this terrain. (C) These ridges capture potential neuronal branches. (D) Dashed curves are union of 1-unstable manifolds.

more challenging [5]. Nevertheless, recovering a hidden graph skeleton (singular 1-manifolds) from low or high-dimensional data has attracted much attention; e.g. in [26, 27, 32, 1, 10, 24, 28]. In general, identifying graph nodes and connections between them can be challenging, especially since often local information is used to make inference or decisions, making it hard to handle noise, non-uniform sampling and gaps in data. To this end, topological methods become useful, as they offer ways to capture the global structure behind data and thus can be robust in detecting junction nodes and their global connectivity. Indeed, there are several algorithms that extract a graph skeleton behind point cloud data (PCD) based on the Reeb graph type topological structure; e.g. [24, 10, 28]. Unfortunately, while such approaches work well when the input points are sampled within a tubular neighborhood of the hidden graph (called under tubular or Hausdorff noise), they do not handle more general noise very well, such as outliers and background noise. The locally-defined principal curve approach [32] on the other hand, can handle noisy data with non-tubular noise, via a ridge-finding strategy using a constraint mean-shift-like procedure. However, the procedure only moves points closer to a graph skeleton without outputting an actual graph.

Recently, there has been a line of work using a persistence-guided discrete Morse theory based approach to reconstruct a 1D graph (or even 2D) skeleton from data; e.g. [14, 25, 34, 36, 38]. In particular, assume that the input is a density field defined on a discretized domain (e.g. a triangulation or a cubic complex). The method uses the discrete Morse (DM) theory to compute the so-called 1-stable manifolds to capture the mountain ridges of the density field and returns these mountain ridges as the extracted graph skeleton; see Figure 1 for a 2D example. Persistent homology is integrated to simplify the density field and thus the resulting 1-stable manifolds. The algorithm based on this idea has been significantly simplified in [18] with theoretical understanding, with theoretical analysis of the output graph. The resulting method (which we will refer to as **DM-graph**) can recover a hidden graph from noisy and non-homogeneous density field, and has already been applied to several applications in 2D/3D [2, 15, 17]. These graphs, along with features naturally computed during the execution of the algorithm, have also been used as input for Graph Neural Networks (GNNs) to generate effective predictive models [7].

However, this algorithm currently assumes that one has *a discretization of the ambient space where data are embedded in*, which becomes prohibitively expensive for data embedded in high-dimensional space, and it also cannot be directly applied to metric data that are not embedded.

New work. We consider the general setting where the input is just a set of points P either embedded in a metric space, say the Euclidean space \mathbb{R}^d , or with pairwise distances (or correlations) given. The previous **DM-graph** does not work in this setting, and as we will explain later, the straightforward extension is not effective for high-dimensional PCDs. In this paper, we extend the idea behind the discrete-Morse based approach beyond density field, as well as combine it with the so-called sparsified weighted Rips filtration of [6] to develop an effective and efficient algorithm to infer graph skeletons of high-dimensional PCDs.

More specifically, in Section 3, we view **DM-graph** reconstruction method from a filtration perspective instead of a density perspective, and thus generalize the **DM-graph** algorithm to work with an arbitrary filtration (which intuitively is a sequence of growing spaces spanned by our input points in our setting). We then prove (Theorem 3.4) that the output of the generalized method contains a so-called *lex-optimal*

persistent cycle basis of the given filtration, thereby showing that the output captures meaningful information w.r.t. the filtration. This result is of independent interest.

We next show how this simple change of view can help us reconstruct the graph skeleton of a set of points P more efficiently and effectively. In particular, the filtration perspective now allows us to combine the DM-based graph reconstruction algorithm with a sparsified weighted Rips filtration scheme proposed by [6], which both improves the quality of the reconstruction and significantly reduces the time complexity. This new graph reconstruction algorithm for PCDs, called DM-PCD, is our second main contribution and presented in Section 4.

Finally, we show experimental results on a range of datasets, and compare with a previous SOA graph reconstruction of [24] and a baseline built directly upon the DM-graph of [18], to demonstrate the effectiveness of our new DM-PCD algorithm. More results are shown in the appendix.

2 Preliminaries and a graph skeletonization algorithm for density field

We now briefly introduce some notions needed to describe the idea behind the DM-graph algorithm of [38, 18] as well as our theoretical results in Section 3. See Appendix A for a much more detailed introduction of preliminaries such as persistent homology and discrete Morse theory.

Simplicial setting. We consider the **simplicial setting**, where the space of interest is modeled by a *simplicial complex* K , consisting of basic building blocks called *simplices*. Intuitively, a geometric d -simplex is the convex combination of $d + 1$ affinely independent vertices: a 0-, 1-, 2-, or 3-simplex is just a vertex, an edge, a triangle, or a tetrahedron. Ignoring the geometry, an *abstract d -simplex* $\sigma = (v_0, \dots, v_d)$ is a set of $d + 1$ vertices. Any subset τ of the vertices of a d -simplex σ gives a *face* of σ , and τ is called a *facet* of σ if its dimension is $d - 1$. For example, a 2-simplex (triangle) spanned by vertices $v_0v_1v_2$ has faces such as edge v_0v_1 or vertex v_2 . A simplicial complex K is a collection of simplices with the property that if a simplex σ is in K , then any of its face must be in K as well. Given a simplicial complex K , its q -*skeleton* K^q consists of all simplices in K of dimension at most q .

2.1 Persistent homology

Given a topological space X , the classical notion of p -*th homology classes* intuitively capture p -dimensional "holes" in X ; i.e., connected components (0D), loops (1D), voids (2D) and their higher dimensional analogs. The p -*th homology group* $H_p(X)$ (under \mathbb{Z}_2 coefficients) is the vector space spanned by such topological features, and its rank, called the p -*th Betti number* $\beta_p(X)$, gives the number of independent topological "holes". We consider simplicial homology in this paper where X is a simplicial complex K . Refer to the Supplementary Materials for a more detailed exposition.

The persistent homology can be viewed as a (modern) multi-scale extension of homology. In particular, instead of considering only the space K itself, imagine we are given an evolution of this space modeled by a *filtration*, which is a sequence of the spaces connected by inclusions: $\mathcal{F} : K_1 \subseteq K_2 \subseteq \dots \subseteq K_m = K$. As the space grows through this filtration, the persistent homology (PH) can track the birth and death of homological features via its induced *persistence module* $\mathbb{P}\mathcal{F} : H_q(K_1) \rightarrow H_q(K_2) \rightarrow \dots \rightarrow H_q(K_m)$, where maps are induced by inclusions. The results are summarized in the so-called *persistence diagram (PD)* $\text{dgm}_p\mathcal{F}$, for $p = 0, 1, \dots$ (dimension): Specifically, $\text{dgm}_p\mathcal{F}$ (e.g, Figure 4 (B)) consists a multiset of points (i.e, points can have multiplicity) such that each $(b, d) \in \text{dgm}_p$ corresponds to the birth time (b) and death time (d) of some p -dimensional homological feature during the filtration \mathcal{F} ; that is, the feature is created when entering K_b but killed (becoming trivial) when entering K_d . Note that d could be ∞ , indicating that a feature is created at time b but never killed (and thus exists in K_m). For this simple setting, the *persistence* of a persistence point (b, d) is defined as its *lifetime* $\text{pers}((b, d)) = |d - b|$.

Simplex-wise filtration, persistence, and negative/positive simplices. Now suppose the input filtration $\mathcal{F} : K_1 \subset \dots \subset K_m$ is *simplex-wise*, namely, it is induced by an ordering $\sigma_1, \dots, \sigma_m$ of simplices in K such that $K_i := \{\sigma_1, \dots, \sigma_i\}$ is the prefix of this sequence. Note that for each i , $K_i = K_{i-1} \cup \{\sigma_i\}$. (In what follows, we sometimes do not differentiate a simplex-wise filtration from the ordering of simplices inducing it.)

In this case, given a persistence point $(b, d) \in \text{dgm}_p \mathcal{F}$, we can in fact associate to it a persistence simplex-pair (σ_b, σ_d) . In other words, the corresponding topological feature was created when adding simplex σ_b to obtain K_b , and killed when adding σ_d to obtain K_d . Simplex σ_b is *positive* as it creates, while σ_d is *negative* as it kills a topological feature.

A common way to induce a filtration is via a descriptor function $\rho : V(K) \rightarrow \mathbb{R}$ given at vertices $V(K)$ of K . For simplicity of presentation, assume that ρ is *injective*. We can extend ρ to a simplex-wise function $\rho : K \rightarrow \mathbb{R}$ by setting $\rho(\sigma) = \max_{v \in \sigma} \rho(v)$. Consider an ordering of simplices $\mathcal{S}_\rho : \sigma_1, \dots, \sigma_m$ that is *consistent with ρ* ; i.e, (i) $\rho(\sigma_i) \leq \rho(\sigma_j)$ for any $i \leq j$ and (ii) for any simplex σ_i , its faces appear before it in the ordering. This order induces the so-called *lower-star filtration* \mathcal{F}_ρ w.r.t. ρ . That is, assume $\rho(v_1) < \rho(v_2) < \dots < \rho(v_n)$. We inspect the domain in increasing values of ρ and the lower-star filtration is essentially obtained by adding each vertex v_i and its lower-star (those simplices incident on v_i with function value at most $\rho(v_i)$) in ascending order of i . The persistence diagram $\text{dgm}_p \mathcal{F}_\rho$ encodes birth and death features during this course. In this case, we modify the persistence to reflect function values: specifically, for a persistence point $(b, d) \in \text{dgm}_p \mathcal{F}_\rho$, we set $\text{pers}((b, d)) = \text{pers}((\sigma_b, \sigma_d)) := |\rho(\sigma_d) - \rho(\sigma_b)|$. Features with large persistence survive for a long range of function values and are considered as more important w.r.t. ρ .

2.2 Graph skeletonization algorithm based on Morse theory

Intuition in the smooth setting. Below we first introduce the intuition behind the original discrete Morse based graph reconstruction algorithm of [38], starting with the smooth setting. We will then describe the discrete setting, and its simplification DM-graph by [18]. First, assume we are given a smooth function $\rho : \Omega \rightarrow \mathbb{R}$ on a hypercube domain Ω in \mathbb{R}^d . View ρ as a density function which concentrates around a hidden geometric graph (e.g, Figure 1 (A) where $\Omega \subset \mathbb{R}^2$). Consider the graph of this function in $\{(x, \rho(x)) \mid x \in \Omega\}$, which is a terrain in \mathbb{R}^{d+1} and which we will refer to as the terrain of ρ ; see Figure 1 (B). Intuitively, the “mountain ridge” of this terrain identifies the hidden graphs, as locally on the hidden graph, the density should be higher than points off it. To capture these mountain ridges, one can use the so-called *1-stable manifolds* of the function ρ as in [36, 38].

Given ρ , the gradient vector at $x \in \Omega$, $\nabla \rho(x) = -[\frac{\partial \rho}{\partial x_1}(x), \dots, \frac{\partial \rho}{\partial x_d}(x)]^T$, consists of partial derivatives w.r.t. orthonormal coordinates x_1, \dots, x_d of \mathbb{R}^d , and specifies the steepest descending direction of ρ at x . See Figure 1 (D). Critical points of ρ are points whose gradient vector vanishes (i.e, is $[0, 0, \dots, 0]^T$). For a smooth function on d -D domain, non-degenerate critical points include minima, maxima, and $d-1$ types of saddle points. An integral line is a maximal curve in Ω whose tangent coincides with the gradient of the function ρ at any point in the curve. Intuitively, this is the flow-line traced out by following the gradient direction at every point. Flow-lines (integral lines) start and end (in the limit) at critical points where critical points vanish. Usually, flow-lines end at minima. However, sometimes they may end at saddles, and the *1-unstable manifold* of a saddle (of index $d-1$) is the union of flow-lines starting at some maximum and ending at this saddle. The union of such 1-unstable manifolds intuitively connect mountain peaks to saddles to peaks etc, bounding and separating different valleys (around minima), and thus can be used to capture mountain ridges.

Hence to compute the graph skeleton of an input density function, one would like to compute the union of 1-unstable manifolds of ρ . Furthermore, input density map ρ may be noisy, and to simplify the graph skeleton, one can use the idea of persistent homology to “remove” noisy critical points and keep only the 1-unstable manifolds corresponding to “important” critical points.

Algorithms in the discrete setting. In practice, often we are only given a discrete approximation of the domain Ω , say we have a triangulation K of Ω , with the density function $\rho : V(K) \rightarrow \mathbb{R}$ only available at vertices $V(K)$. To simulate the idea introduced above, [38] uses discrete Morse theory [21, 23]. Due to space limit, here we only describe its high level components, and refer to the Supplementary Materials for details on both discrete Morse theory and the original persistence-guided discrete Morse based graph reconstruction algorithm introduced in [38].

Intuitively, the algorithm aims to maintain the so-called *discrete gradient vector field*, which is analogous to the gradient vector field in the smooth setting. For technical reason, the *1-stable manifolds*, analogous to the “valley ridges”, of the function $\rho' = -\rho$, are computed instead of the 1-unstable manifolds induced by ρ . Such 1-stable manifolds turn out to be a union of vertex-edge paths in the discrete Morse theory; specifically, a vertex-edge path is a certain sequence of alternating vertices and edges $v_0, e_1, v_1, e_2, \dots, v_k$ where $v_i \neq v_{i+1}$ are the two endpoints of edge e_{i+1} , for any $i \in [0, k-1]$. The use of 1-stable manifolds instead of 1-unstable

manifolds also has the consequence that the algorithm only needs the 2-skeleton of the triangulation K of domain $\Omega \subseteq \mathbb{R}^d$ as input, no matter how large d might be. In other words, from now on we assume that K is the 2-skeleton of the d -dimensional domain Ω of interests, consisting of vertices, edges and triangles.

Furthermore, the persistent homology induced by the lower-star filtration of function $\rho' = -\rho$ is used to pair up simplices in K , and those with low-persistence (smaller than a threshold δ) are simplified. In the end, only the 1-stable manifolds w.r.t. important critical edges (corresponding to index-1 saddles in the smooth setting) with persistence $> \delta$ will be collected as the output graph skeleton.

It is later shown in [18] that this algorithm can be further significantly simplified to `DM-graph()` shown in Algorithm 3. The input includes the 2-skeleton $K = (V, E, T)$ of a triangulation of Ω (where V, E , and T stand for the set of vertices, edges and triangles, respectively), $\rho : V(K) \rightarrow \mathbb{R}$ is a density function only accessible at vertices $V(K)$ of K , and a simplification threshold $\delta \geq 0$.

Algorithm 1: `DM-graph(K, ρ, δ)`

Input: Triangulation $K = (V, E, T)$, density function $\rho : V(K) \rightarrow \mathbb{R}$, persistence threshold δ

Output: A graph skeleton G_δ

(Step 1) Compute persistence pairing \mathcal{P} induced by the lower star filtration w.r.t. $-\rho$,

(Step 2) Set $\mathcal{T}_\delta := \{e \in E \mid e \text{ is negative and } \text{pers}(e) \leq \delta\}$

For each component (tree) T in \mathcal{T}_δ , set its root to be $r(T) := \text{argmin}_{v \in T} -\rho(v)$.

(Step 3) Let $\pi_T(x, y)$ be the tree path from x to y in a tree T . Output:

$$G_\delta = \bigcup_{e=(u,v), \text{pers}(e) > \delta} \{e \cup \pi_{T_i}(u, r(T_i)) \cup \pi_{T_j}(v, r(T_j)) \mid u \in T_i, v \in T_j \text{ in } \mathcal{T}_\delta\}. \quad (1)$$

Note that while the output of this algorithm is the same as the original discrete Morse based algorithm of [38], it no longer incurs any notion from discrete Morse theory. In particular, it turns out \mathcal{T}_δ constructed in (Step 2) is necessarily a *spanning forest*, which is why we can talk about each component tree T in \mathcal{T}_δ . This spanning forest contains sufficient information about a simplified discrete gradient vector field as in the original algorithm. In (Step 3), we then collect the 1-stable manifolds for only critical edges with $\text{pers} > \delta$ (corresponding to important saddles in the smooth setting), and their 1-stable manifolds turn out to be the union of tree paths as specified in Eqn (5). Note that (Step 2, 3) can be implemented in time linear to the number of vertices and edges in K .

3 A generalized DM-based graph skeletonization algorithm and optimality

3.1 Filtration perspective of DM-graph algorithm

Now suppose instead of a triangulation of a d -D domain Ω , we have an arbitrary simplicial complex K – our algorithm only needs its 2-skeleton $K = (V, E, T)$. Suppose further that there is a simplex-wise function $\hat{\rho} : K \rightarrow \mathbb{R}$ that sends each simplex $\sigma \in K$ to a real number $\hat{\rho}(\sigma)$. Let $\Pi_{\hat{\rho}} := \langle \sigma_1, \dots, \sigma_N \rangle$ be an ordered sequence of simplices of K that is *consistent with* $\hat{\rho}$ (see end of Section 2.1), and let $\mathcal{F}_{\hat{\rho}}$ be the simplex-wise filtration of K induced by this order $\Pi_{\hat{\rho}}$. (We will describe in Section 4 how to set up this filtration in the graph skeletonization from point cloud data setting.) We now generalize algorithm `DM-graph()` to the following `extDM-graph()`, where essentially, only (Step 1) differs by taking an arbitrary simplex-wise filtration $\mathcal{F}_{\hat{\rho}}$, which we state in Algorithm 2 for clarity.

It is easy to verify that the original `DM-graph(K, ρ, δ)` algorithm is a special case of the above algorithm, where we set $\mathcal{F}_{\hat{\rho}}$ in `extDM-graph($K, \mathcal{F}_{\hat{\rho}}, \delta$)` to be the lower-star filtration induced by the vertexwise function $\rho' = -\rho : V(K) \rightarrow \mathbb{R}$; specifically, for any simplex $\sigma \in K$, set $\hat{\rho}(\sigma) := \max_{v \in \sigma} -\rho(v)$. The difference between our `extDM-graph()` algorithm and the original algorithm is rather minor. However, we will see that this change of perspective (from density-function based view to arbitrary filtration-based view) significantly broadens the applicability of this algorithm. In particular, in Section 4 we will show how this then can be combined with

Algorithm 2: extDM-graph($K, \mathcal{F}_{\hat{\rho}}, \delta$)

Input: Arbitrary simplex-wise filtration $\mathcal{F}_{\hat{\rho}}$ of a simplicial complex $K = (V, E, T)$, threshold δ

Output: A reconstructed graph G_{δ}

(Step 1) Compute persistence pairings w.r.t. $\text{dgm}\mathcal{F}_{\hat{\rho}}$

(Step 2) + (Step 3) are exactly the same as in algorithm DM-graph

weighted Rips sparsification strategy to reconstruct a hidden graph skeleton of high-dimensional points data. But first, in what follows, we provide some characterization of the graph skeleton output by extDM-graph. Specifically, we show that the output of extDM-graph() contains the so-called *lex-optimal* cycle basis of K w.r.t. important 1D homological features in $\text{dgm}_1\mathcal{F}_{\hat{\rho}}$ (in the sense that their persistence is $> \delta$). To make this statement more precise, we now introduce some relevant notations, following [13, 16, 39]. Intuitively, a 1-cycle is a collection of edges forming more or more closed loops, and a d -cycle is a d -D analog of it (refer to the Supplementary Materials for formal definitions).

Definition 3.1 (Persistent cycles [16]). *Let \mathcal{F} be a simplexwise filtration of K induced by the ordered sequence of simplices $\sigma_1, \dots, \sigma_N$, and $\text{dgm}_q\mathcal{F}$ its resulting q -th persistence diagram. Given a point $\mathbf{p} = [b, d] \in \text{dgm}_q\mathcal{F}$, a q -cycle γ is a persistent q -cycle w.r.t. \mathbf{p} if and only if the following holds: (i) if $d \neq \infty$, γ is a cycle in K_b containing σ_b , and γ is not a boundary in K_{d-1} but becomes a boundary in K_d ; and (ii) otherwise if $d = \infty$, then γ is a cycle in K_b containing σ_b .*

Given a subset $D = \{\mathbf{p}_1, \dots, \mathbf{p}_r\} \subseteq \text{dgm}_q\mathcal{F}$ with $r = |D|$, we say that a set of cycles $\{\gamma_1, \dots, \gamma_r\}$ form a persistent cycle-basis for D if γ_i is a persistence cycle w.r.t. \mathbf{p}_i for all $i \in [1, r]$.

Roughly speaking, a persistent cycle γ w.r.t. a persistence point $\mathbf{p} = [b, d]$ is created at b and killed at d , and can be thought of a representative of the homological feature captured by point $\mathbf{p} \in \text{dgm}\mathcal{F}$. A persistent cycle basis w.r.t. $D \subset \text{dgm}\mathcal{F}$ correspond to representative cycles captured by points in D .

Lexicographic optimal cycles are introduced in [12, 13]. We will extend them to the persistence version. Given a simplex-wise filtration \mathcal{F} of K induced by an ordering of simplices $\sigma_1, \dots, \sigma_N$, we set $\text{ind}(\sigma)$ as the order it appears in \mathcal{F} ; i.e, $\text{ind}(\sigma_i) = i$.

Definition 3.2 (Lexicographic order [13]). *Given two q -cycles $C_1, C_2 \in \mathcal{C}_q(K)$, we say that $C_1 \preceq C_2$ if either (i) $C_1 + C_2 = 0$ or (ii) otherwise, the simplex $\sigma_{\max} := \text{argmax}_{\sigma \in C_1 + C_2} \text{ind}(\sigma)$ is from C_2 . If (ii) holds, we say that $C_1 \prec C_2$, i.e., C_1 is smaller than C_2 in lexicographic order. Intuitively, $C_1 \preceq C_2$ if simplices in C_1 comes “earlier” than C_2 in the filtration order.*

Definition 3.3 (Lex-optimal persistent cycle and cycle-basis). *Given a persistence point $\mathbf{p} = [b, d] \in \text{dgm}_q\mathcal{F}$, a q -cycle γ is a lexicographic-optimal persistent cycle w.r.t. \mathbf{p} (or lex-opt persistent cycle in short), if (i) γ is a persistent cycle w.r.t. \mathbf{p} ; and (ii) among all persistence cycles w.r.t. \mathbf{p} , γ has the smallest lexicographic order. We say that $\Gamma = \{\gamma_1, \dots, \gamma_r\}$ forms a Lex-optimal persistent cycle basis for a multiset $D = \{\mathbf{p}_1, \dots, \mathbf{p}_r\} \subseteq \text{dgm}_q\mathcal{F}$ if γ_i is a Lex-optimal persistence cycle w.r.t \mathbf{p}_i for all $i \in [1, r]$.*

Given a q -th persistence diagram $\text{dgm}_q\mathcal{F}$ and a threshold δ , let $\text{dgm}_q\mathcal{F}(\delta) \subseteq \text{dgm}_q\mathcal{F}$ denote the subset of points in $\text{dgm}_q\mathcal{F}$ whose persistence is larger than δ (intuitively, these correspond to important features). Our first main result is the following theorem (proof in the next section).

Theorem 3.4. *(i) G_{δ} as constructed w.r.t. a simplex-wise filtration \mathcal{F}_{ρ} contains a Lex-optimal persistence cycle basis for $\text{dgm}_1\mathcal{F}_{\rho}(\delta)$, and (ii) the first Betti number of G_{δ} equals $|\text{dgm}_1\mathcal{F}_{\rho}(\delta)|$.*

The above theorem suggests that the output graph G_{δ} by our algorithm extDM-graph() contains “best” loops whose homology classes have large persistence and whose edges come *as early as possible in the filtration*. In particular, imagine that important edges or more faithful edges come early in the filtration, then the output graph contains those loops with large persistence ($> \delta$) and formed by more faithful edges whenever possible. In the graph reconstruction from PCDs application in the next section, intuitively, if edges from high-density region comes into the filtration first, then the resulting output graph will use such edges whenever possible. See Figure 4 (A) to (D).

3.2 Proof of Theorem 3.4

We assume that K is connected. If it is not, then we will perform the following arguments to each connected component of K . Now recall that $\mathcal{T}_\delta := \{e \in E \mid e \text{ is negative and } \text{pers}(e) \leq \delta\}$ consists of all negative edges with persistence at most δ (from (Step 2) of algorithm `extDM-graph`). It is shown in [18] that \mathcal{T}_δ consists of a set of trees. Set

$$\begin{aligned} E_\delta^+ &:= \{e \in E \mid e \text{ is positive and } \text{pers}(e) > \delta\}, \text{ and} \\ E_\delta^- &:= \{e \in E \mid e \text{ is negative and } \text{pers}(e) > \delta\}. \end{aligned}$$

Set $\widehat{G}_\delta = \mathcal{T}_\delta \cup G_\delta$. It is easy to see that by construction of G_δ , which consists of edges in $E_\delta^- \cup E_\delta^+$ with certain tree paths in \mathcal{T} , we that

$$\widehat{G}_\delta = \mathcal{T}_\delta \cup G_\delta = \mathcal{T}_\delta \cup E_\delta^- \cup E_\delta^+. \quad (2)$$

We prove Theorem 3.4 in two steps, laid out in the following two lemmas.

Lemma 3.5. *Statements (i) and (ii) in Theorem 3.4 holds for \widehat{G}_δ . That is: (i') \widehat{G}_δ as constructed w.r.t. a simplex-wise filtration \mathcal{F}_ρ contains a Lex-optimal persistence cycle basis for $\text{dgm}_1 \mathcal{F}_\rho(\delta)$, and (ii') the first Betti number of \widehat{G}_δ equals $|\text{dgm}_1 \mathcal{F}_\rho(\delta)|$.*

Lemma 3.6. *\widehat{G}_δ deformation contracts to G_δ .*

Our theorem then follows from these two lemmas. Specifically, we will use the graph \widehat{G}_δ as a proxy: Lemma 3.5 states that the desired results hold for \widehat{G}_δ . Lemma 3.6 then relates \widehat{G}_δ to G_δ . In particular, as both \widehat{G}_δ and G_δ are graphs, this lemma implies that any simple cycle in \widehat{G}_δ must be present in G_δ as well. Theorem 3.4 then follows. What remains is to prove these two lemmas, which we present in the two subsections below.

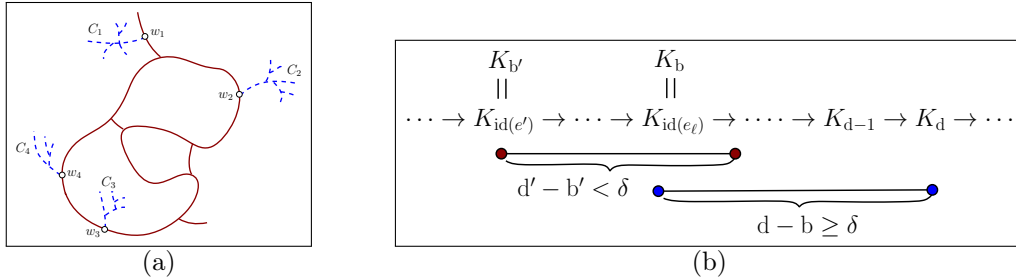


Figure 2: (a) The solid red curve is G_δ , while dashed trees are components in $\widehat{G}_\delta \setminus G_\delta$. The closure of each component C_i connects to G_δ at one point w_i , and thus its closure can deformation retract to $w_i \in G_\delta$. (b) As $\text{pers}(e') = d' - b' \leq \delta$, and $\text{pers}(e_\ell) = d - b > \delta$, and $b' (= \text{ind}(e')) \leq b$, it then follows that the persistent cycle $C' = \pi(u, v) + e'$ must become a boundary in the simplicial complex K_{d-1} , which in turn leads to that $[\gamma'] = [\gamma^*]$ in K_{d-1} .

3.2.1 Proof of Lemma 3.5

Let $\text{dgm}_1 \mathcal{F}_\rho(\delta) = \{p_1, \dots, p_g\}$. By the definition of positive and negative edges, we know:

- (C1). $\widehat{\mathcal{T}} = \mathcal{T}_\delta \cup E^-$ is a spanning tree of K .
- (C2). By the definition of positive edges, E_δ^+ contains exactly those edges whose addition create the persistence points in $\text{dgm}_1 \mathcal{F}_\rho(\delta)$. In other words, $g = |E_\delta^+|$ and we can order edges in $E_\delta^+ = \{e_1, \dots, e_g\}$ so that for any $\ell \in [1, g]$, $p_\ell = [\text{ind}(e_\ell), d_\ell]$: i.e., the birth-time of p_ℓ corresponds to the insertion of edge e_ℓ in the simplicial complex $K_{\text{ind}(e_\ell)}$.

Furthermore, the addition of each positive edge $e_\ell \in E_\delta^+$ creates a cycle in the spanning tree $\widehat{\mathcal{T}}$ (as e_ℓ is not a tree edge), As $\widehat{G}_\delta = \widehat{\mathcal{T}} \cup E^+$, we thus have $\beta_1(\widehat{G}_\delta) := \text{rank}(\mathbf{H}_1(\widehat{G}_\delta))$ is the same as $g = |\text{dgm}_1 \mathcal{F}_\rho(\delta)|$. This proves part (ii') in Lemma 3.5 for the graph \widehat{G}_δ .

We now prove part (i') of Lemma 3.5. Consider any $e_\ell \in E_\delta^+$, and let γ^* denote a lex-opt persistent cycle of the corresponding persistence point $\mathbf{p}_\ell = [\mathbf{b}, \mathbf{d}]$. By Definitions 3.1 and 3.3 in the main paper, γ^* necessarily contains e_ℓ , and all other edges in γ^* has an index smaller than $\text{ind}(e_\ell)$. We will next prove that γ^* is in \widehat{G}_δ , that is, $\gamma^* \subseteq \widehat{G}_\delta$.

In particular, take any edge $e' \in \gamma^*$ with $e' \neq e_\ell$, we will show that $e' \in \widehat{G}_\delta$.

- If e' is negative, then this is trivially true as $e' \in \widehat{\mathcal{T}} \subseteq \widehat{G}_\delta$.
- If e' is positive but with persistence $\text{pers}(e') > \delta$, then it is also true as $e' \in E_\delta^+ \subseteq \widehat{G}_\delta$.
- So what remains is the case when $e' = (u, v)$ is positive but with $\text{pers}(e') \leq \delta$. However, we will show that this case cannot happen, which will then imply that $e' \in \widehat{G}_\delta$.

Assume this case happens for edge e' . Then let $C_{e'} (= \pi(u, v) + e') \subset K_{\text{ind}(e')}$ be a persistent cycle w.r.t. the persistence point $[\mathbf{b}' = \text{ind}(e'), \mathbf{d}']$ generated by e' . First, as the path (1-chain) $\pi(u, v)$ is contained in $K_{\text{ind}(e')}$, all edges in $\pi(u, v)$ have an index less than that of e' . This means that the cycle $\gamma' = \gamma^* - e' + \pi(u, v)$ is necessarily smaller than γ^* in lexicographic order. We now claim that γ' is also a persistent cycle w.r.t. $\mathbf{p}_\ell = [\mathbf{b}, \mathbf{d}]$ (i.e., the persistence point corresponds to the positive edge e_ℓ).

Indeed, as γ^* is a persistent cycle w.r.t. \mathbf{p}_ℓ , we know that $\text{ind}(e') < \text{ind}(e_\ell) = \mathbf{b}$. Recall that the persistence point corresponds to the positive edge e' is $[\mathbf{b}' = \text{ind}(e'), \mathbf{d}']$. As $\text{pers}(e_\ell) = \rho(\mathbf{d}) - \rho(\mathbf{b}) > \delta$ while $\text{pers}(e') = \rho(\mathbf{d}') - \rho(\mathbf{b}') \leq \delta$, it then follows that $\mathbf{d}' < \mathbf{d}$. (See Figure 2 (b) for illustrations of these notations.) Hence we know that it is necessary that the cycle $\pi(u, v) + e'$ becomes boundary in $K_{\mathbf{d}-1}$. In other words, in $K_{\mathbf{d}-1}$, the two cycles γ^* and γ' are homologous. It is then easy to verify that γ' must be a persistent cycle for \mathbf{p}_ℓ as well.

Since γ' is also a persistent cycle for \mathbf{p}_ℓ and is lexicographically smaller than γ^* , this contradicts our assumption that γ^* is a lex-opt persistent cycle for \mathbf{p}_ℓ . Hence no edge positive edge $e' \in \gamma^*$ with $\text{pers}(e') < \delta$ can be in γ^* .

Assume this case happens for edge e' . Then let $C_{e'} (= \pi(u, v) + e') \subset K_{\text{ind}(e')}$ be a persistent cycle w.r.t. the persistence point $[\mathbf{b}' = \text{ind}(e'), \mathbf{d}']$ generated by e' . First, as the path (1-chain) $\pi(u, v)$ is contained in $K_{\text{ind}(e')}$, all edges in $\pi(u, v)$ have an index less than that of e' . This means that the cycle $\gamma' = \gamma^* - e' + \pi(u, v)$ is necessarily smaller than γ^* in lexicographic order. We now claim that γ' is also a persistent cycle w.r.t. $\mathbf{p}_\ell = [\mathbf{b}, \mathbf{d}]$ (i.e., the persistence point corresponds to the positive edge e_ℓ).

By the above case analysis, any edge $e' \in \gamma^*$ must be in \widehat{G}_δ . It then follows that $\gamma^* \subseteq \widehat{G}_\delta$. As this argument holds for any edge in E_δ^+ , we thus have proven (i'). This finishes the proof of Lemma 3.5.

3.2.2 Proof of Lemma 3.6

First, by construction of \widehat{G}_δ (Eqn (2)), we have that $G_\delta \subseteq \widehat{G}_\delta$, and all edges in $\widehat{G}_\delta \setminus G_\delta$ must come from \mathcal{T}_δ . Now recall $\widehat{\mathcal{T}} = \mathcal{T} \cup E^-$, which is a spanning tree of K . Given an arbitrary tree T and two nodes $u, v \in T$, let $\pi_T(u, v)$ denote the unique tree path from u to v in T .

Claim 3.7. *Given any tree rooted tree T with root $r(T)$ and two nodes $u, v \in T$, we have that $\pi_T(u, v) \subseteq \pi_T(u, r(T)) \cup \pi_T(v, r(T))$.*

Proof. If u and v have ancestor / descendent relation, say u is ancestor of v , then it is clear that $\pi_T(u, v) \subseteq \pi_T(v, r(T))$, and the claim then follows. Otherwise, let w be the common ancestor of u and v . It can again be verified that in this case, $\pi_T(u, w) \subseteq \pi_T(u, r(T))$, $\pi_T(v, w) \subseteq \pi_T(v, r(T))$, while $\pi_T(u, v) = \pi_T(u, w) \cup \pi_T(w, v)$. The claim thus follows. \square

Given any vertex v , suppose it is in the tree $T \in \mathcal{T}_\delta$. We denote $\text{path}_{\mathcal{T}_\delta}(v) := \pi_T(v, r(T))$ to be the path from v to the root $r(T)$ of T . Recall that G_δ is constructed by, for any edge $e = (u, v) \in E^- \cup E^+$, adding $e \cup \text{path}_{\mathcal{T}_\delta}(u) \cup \text{path}_{\mathcal{T}_\delta}(v)$ into G_δ .

Claim 3.8. For each edge $e = (u, v) \in E_\delta^+$, set $\gamma = e \cup \pi_{\widehat{\mathcal{T}}}(u, v)$. Then the cycle γ must be contained in G_δ .

Proof. Consider the path $\pi = \pi_{\widehat{\mathcal{T}}}(u, v)$: it will be broken into $k \geq 0$ maximally connected pieces from \mathcal{T}_δ , connected by edges in $E^- \cup E^+$. If $k = 0$, we are done, because this means that u, v are contained in the same tree T in \mathcal{T} , and it then follows from Claim 3.7 that

$$\pi = \pi_T(u, v) \subseteq \text{path}_{\mathcal{T}_\delta}(u) \cup \text{path}_{\mathcal{T}_\delta}(v) \subseteq G_\delta.$$

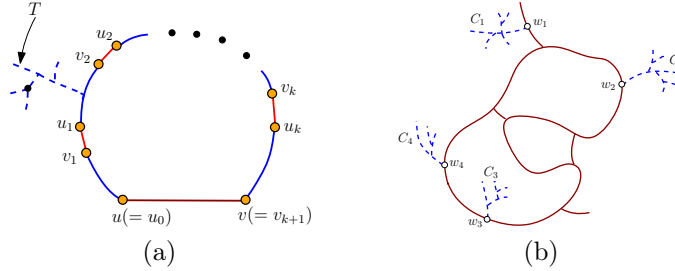


Figure 3: (a) The path $\pi = \pi(u, v)$ is broken into $k + 1$ pieces, each of which (blue subcurves) is a maximal connected component in $\pi \cap \mathcal{T}_\delta$, while the connecting edges (red edges (v_i, u_i) 's) must come from $E_\delta^- \cup E_\delta^+$. (b) The solid red curve is G_δ , while dashed trees are components in $\widehat{G}_\delta \setminus G_\delta$. The closure of each C_i connects to G_δ at one point w_i , and thus its closure can deformation retract to w_i .

So assume that $k > 0$, and the edges connecting these pieces from \mathcal{T}_δ are $e_1 = (v_1, u_1), \dots, e_k = (v_k, u_k)$ from u to v along π ; see Figure 3 (a). Set $u_0 = u$ and $v_{k+1} = v$. It then follows that for any $i \in [0, k]$, u_i is connected to v_{i+1} within some tree, say $T \in \mathcal{T}_\delta$. It then follows from Claim 3.7 that the portion of π from u_i to v_{i+1} must be contained in $\text{path}(u_i) \cup \text{path}(v_{i+1})$. Applying this for all $i \in [0, k]$, it follows that

$$\begin{aligned} \pi &\subseteq \left[\bigcup_{i \in [0, k]} (\text{path}(u_i) \cup \text{path}(v_{i+1})) \right] \bigcup (e_1 \cup e_2 \cdots \cup e_k) \\ &= (\text{path}(u) \cup \text{path}(v)) \bigcup (e_1 \cup \text{path}(v_1) \cup \text{path}(u_1)) \bigcup \cdots \bigcup (e_k \cup \text{path}(v_k) \cup \text{path}(u_k)). \end{aligned}$$

As all edges e_1, \dots, e_k and e are all in $E^- \cup E^+$, it then follows that $\pi \subseteq G_\delta$ and thus $\gamma = e \cup \pi \subseteq G_\delta$. \square

Claim 3.9. $\beta_0(G_\delta) = \beta_0(\widehat{G}_\delta)$, and $\beta_1(G_\delta) = \beta_1(\widehat{G}_\delta)$.

Proof. That $\beta_1(G_\delta) = \beta_1(\widehat{G}_\delta)$ follows immediately from Claim 3.8. We now prove that G_δ and \widehat{G}_δ also has the same connected component. Note that we have already assumed that K is connected, and thus \widehat{G}_δ is connected as it contains a spanning tree $\widehat{\mathcal{T}}$ of K . So what remains is to show that G_δ is connected.

Assume G_δ is not connected, and let C_1, C_2 be two components of G_δ . Let $e_1 \in C_1$ be an arbitrary edge from $C_1 \cap (E^- \cup E^+)$: Note that such an edge must exist, as otherwise C_1 will not be in G_δ . Similarly, let $e_2 \in C_2 \cap (E^- \cup E^+)$. Let u be an endpoint of e_1 while w be an edge point of e_2 . We know that u and w are connected in \mathcal{T}_δ by path $\pi = \pi_{\mathcal{T}_\delta}(u, w)$. We can then use an argument similar to the one in the proof of Claim 3.8 to show that this path in fact has to be in G_δ ; thus C_1 and C_2 cannot be disconnected in G_δ . So G_δ must be connected as well, and this finishes the proof of the claim. \square

Now let C_1, \dots, C_s be the components of $\widehat{G}_\delta \setminus G_\delta$, and for each $i \in [1, s]$, let \bar{C}_i be the closure of C_i . We claim that $\bar{C}_i \setminus C_i$ can contain only one vertex, say w_i . See Figure 3 (b). Indeed, as $\widehat{G}_\delta \setminus G_\delta \subseteq \mathcal{T}_\delta$, each \bar{C}_i is simply connected (i.e, it is a subtree of some tree in \mathcal{T}_δ). Suppose $\bar{C}_i \setminus C_i$ contains at least two vertices, say w and w' . As \bar{C}_i is connected, there is a path $\pi_{\bar{C}_i}(w, w')$ connecting w to w' in \bar{C}_i . On the other hand, as G_δ is connected (Claim 3.9), there is another path $\pi_{G_\delta}(w, w')$ connecting w and w' . This gives rise to a cycle $\gamma = \pi_{\bar{C}_i}(w, w') \cup \pi_{G_\delta}(w, w')$ in \widehat{G}_δ , and this cycle is not in G_δ . This however contradicts to what we just proved that $\beta_1(G_\delta) = \beta_1(\widehat{G}_\delta)$. Hence this cannot happen.

Hence \bar{C}_i can only connect to G_δ via one point w_i as illustrated in Figure 3 (b). It then follows that \widehat{G}_δ deformation retracts to G_δ by contracting each subtree \bar{C}_i to the point w_i . This finishes the proof of Lemma 3.6.

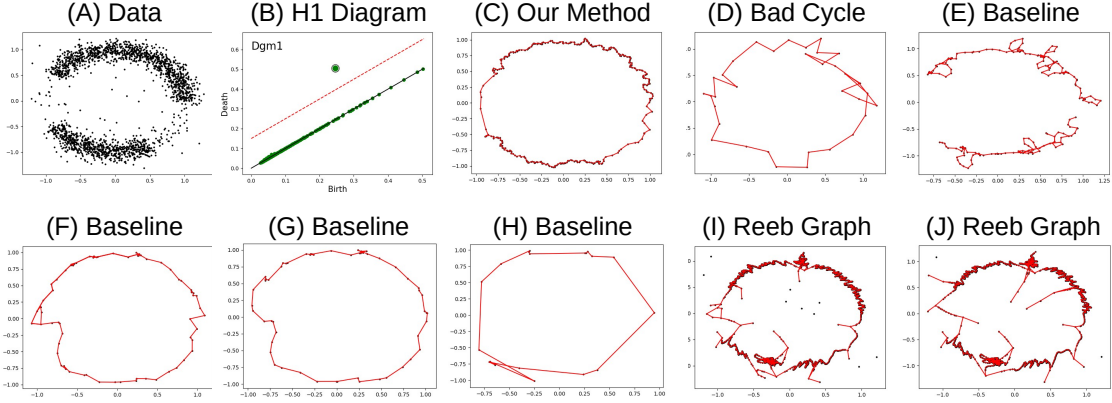


Figure 4: (A) Noisy sample of a circle. (B) 1-D persistence diagram w.r.t. our later sparse DTM-Rips filtration. Persistence points are green. Only one point (big point) \mathbf{p} has persistence larger than some threshold δ (above the red dotted line). (C) Output of our DM-PCD method, which is a lex-optimal persistent cycle w.r.t. the only high persistence point \mathbf{p} in (B). (D) shows a "bad" persistent cycle w.r.t. the same high persistence point \mathbf{p} . In contrast, our output in (C) uses good (high density) edges whenever possible. (E) – (H) are outputs from the baseline algorithm using different radius r . (E) $r = 0.1$: At this scale, the number of simplices in $\text{rips}^r(P)$ is on par with the total #simplices in our sparse DTM-Rips. However, the underlying shape (circle) is not yet captured. (F) $r = 0.2$: There are spurious loops that cannot be simplified via persistence. (G) $r = 0.25$: The circle is recovered; however, the size of $\text{rips}^r(P)$ is now 20 times that of our sparse DTM-Rips filtration. (H) $r = 1.05$: The output, while still a circle, loses geometric details. (I) is an output from ReebRecon using $\text{rips}^r(P)$ with different radius $r = .2$, which includes a spurious loop. (J) is an output from ReebRecon using $\text{rips}^r(P)$ with $r = .25$. Although the circle is captured, there is a significant amount of noise.

4 DM-PCD: Graph reconstruction for PCD via sparse weighted-Rips

Now suppose we are given a point cloud dataset $P \subset \mathbb{R}^d$ and we wish to compute a graph skeleton of P . Our algorithm can be easily extended to the case where these points P are not embedded with only pairwise distances (or similarity) given.

A baseline approach. A natural approach is to (i) build a simplicial complex K from P to "approximate" the space behind P , (ii) estimate a density function ρ at $P = V(K)$, and (iii) then perform algorithm **DM-graph**. A reasonable choice for K is the so-called Rips complex $\text{rips}^r(P) := \{(p_{i_0}, \dots, p_{i_k}) \mid \|p_{i_j} - p_{i_{j'}}\| \leq r\}$: Intuitively, an edge $(p, q) \in \text{rips}^r(P)$ if the distance between points $p, q \in P$ is at most r . A triangle is in $\text{rips}^r(P)$ if all three edges are in, and similarly for higher-dimensional simplices. However, we only need 2-skeleton of $\text{rips}^r(P)$, which we still denote by $\text{rips}^r(P)$. We refer to it as algorithm **baseline** where we use the $\text{rips}^r(P)$ as choice of complex K , that is, we perform **DM-graph**($\text{rips}^r(P), \rho, \delta$).

Challenges with baseline. This baseline approach faces several challenges. (C-1) It is usually hard to choose the right radius r and the topology of $\text{rips}^r(P)$ crucially decides the final output graph: see Figure 4, where if r is too small, the shape is not yet captured by $\text{rips}^r(P)$; for larger r , there can be spurious topological features (extra loops) in K which cannot be simplified by persistence (as these loops are generated by edges with infinity persistence). There is also the issue that even if one has found a radius r value such that $\text{rips}^r(P)$ can provide the correct topology, the geometry of the graph skeleton computed by this baseline algorithm may lose resolution (e.g, Figure 4 (F)).

(C-2) Furthermore, points may be sampled at different resolution, hence there may not exist a single good r that can capture all features; see Figure 5. (C-3) Even for moderate radius r , the size of Rips complex becomes large (this issue becomes even more severe for high-dimensional PCDs), which renders the persistence computation infeasible. (C-4) Finally, the Rips complex is not effective at handling background noise; see Figure 5 (E) and (G), where even though the hidden space consists of 5 independent cycles (see Section 5), with much background noise, even a small radius r makes the Rips complex connect these noisy points and lose the hidden structure. Removing low-density points can help; however in general that can be challenging

when the density distribution is non-uniform.

A DTM-Rips based approach. The Rips complex is defined based on the Euclidean distance between input points, and does not handle noise or non-uniform point samples well. The *distance-to-measure* (DTM) distance is introduced in [9] to provide a more robust way to produce distance field for noisy points. We use the work of [6] to induce a weighted Rips complex from DTM distances, which we now describe briefly. In particular, given a set of points (P, \mathbf{d}_P) equipped with metric d_P (for points $P \subset \mathbb{R}^d$, \mathbf{d}_P is the Euclidean distance in \mathbb{R}^d). For a fixed integer parameter $k > 0$, let $kNN(p)$ denote the set of k -nearest neighbor of p in P under metric \mathbf{d}_P . For each $p \in P$, we set (*DTM-induced*) weight w_p as $w_p = \sqrt{\frac{1}{k} \sum_{q \in kNN(p)} \mathbf{d}_P^2(p, q)}$, and the *weighted radius of p at scale α* as $r_p(\alpha) = \sqrt{\alpha^2 - w_p^2}$. Now given a simplex $\sigma = \{p_{i_0}, \dots, p_{i_s}\}$, we define $\rho_w(\sigma)$ to be

$$\rho_w(\sigma) = \min\{\alpha' \mid w_{p_{i_j}} \leq \alpha', \text{ and } \mathbf{d}_P(p_{i_j}, p_{i_{j'}}) \leq r_{p_{i_j}}(\alpha') + r_{p_{i_{j'}}}(\alpha'), \forall j \neq j' \in [0, s]\}.$$

This gives an ordering of all possible simplices formed by points in P (again, only simplices of dimension at most 2 are needed), and the resulting filtration is called *DTM-Rips filtration* \mathcal{F}_{ρ_w} . Equivalently, consider the DTM-weighted Rips complex $wRip^\alpha(P)$ at scale r defined as: $wRip^r(P) = \{\sigma = \{p_{i_0}, \dots, p_{i_s}\} \mid \rho_w(\sigma) \leq r\}$. The sequence of $wRip^r(P)$ with increasing scales $r = [0, \infty)$ gives rise to the filtration \mathcal{F}_{ρ_w} . The weight w_p is a certain average distance to the k NN of p and thus intuitively an inverse density estimator (high density points have low weight). Given two points $p, q \in P$, the edge $\sigma = (p, q)$ has **smaller** $\rho_w(\sigma)$ if p and q has lower weight (thus **higher density**). Simplices spanned by **higher** density points will enter **earlier** into the filtration \mathcal{F}_{ρ_w} .

DM-PCD: Incorporating data sparsification. However, the size of weighted Rips can still be large. To this end, we deploy the sparsified version of DTM-Rips developed by Buchet et al. in [6]. The resulting filtration is denoted by *sparse DTM-Rips* $\widehat{\mathcal{F}}_{\rho_w}(\varepsilon)$ which uses a sparsification parameter $\varepsilon > 0$. We refer readers to [6] for details of its construction, as well as the guarantee in terms of approximating the persistence diagram $\text{dgm}\mathcal{F}_{\rho_w}$. Our final graph skeletonization algorithm for points cloud data (PCD), denoted by $\text{DM-PCD}(P, k, \varepsilon, \delta)$, consists of only two simple steps:

- (Step 1). Computes the sparse DTM-Rips filtration $\widehat{\mathcal{F}}_{\rho_w}(\varepsilon)$ using parameters k (to compute DTM-weights of points) and ε (for sparsification).
- (Step 2). Apply $\text{extDM-graph}(K, \widehat{\mathcal{F}}_{\rho_w}(\varepsilon), \delta)$ to compute the graph skeleton of P , where K is given implicitly as all simplices in $\widehat{\mathcal{F}}_{\rho_w}(\varepsilon)$.

Intuitively, using the DTM-weight alleviates the problem of noisy points (challenge (C-4)), using sparsification addresses the issue of size (challenge (C-3)), while using the entire sparse DTM-Rips filtration allows us to use all radii/scales (instead of a Rips complex at a fixed radius r as in baseline), thereby addressing challenges (C-1) and (C-2). Furthermore, while at a larger radius, the filtration will include edges and triangles spanned by far-away points, note that our Theorem 3.4 guarantees that we will output those important loop features using edges that come in as early as possible, i.e., spanned by higher density points (with smaller ρ_w values) whenever possible. This allows our DM-PCD algorithm to captures hidden graph across different scales. See Figure 5.

5 Experimental results

All experiments are run on a single node of GPU cluster with 2 x 11GB NVIDIA RTX2080Ti, 192 GB of RAM, 4.2TB SSD, and 2 x 64-bit 18-core Intel Xeon GOLD 6140 Scalable CPU. For both DM-graph and extDM-graph , persistence computation is the bottleneck, as other than this step, the algorithm takes only linear time. We compare our DM-PCD algorithm with the baseline algorithm using a fixed Rips complex (see Section 4), and with one SOA graph skeletonization algorithm based on Reeb graph [24] (referred to as ReebRecon below). We test on two synthetic point sets and three real datasets. Unless otherwise specified, we use $k = 15$ and $\varepsilon = .99$ in our $\text{DM-PCD}(P, k, \varepsilon, \delta)$; while the persistence simplification threshold δ depends on the point set at hand. For baseline and ReebRecon , we report the results of best parameters we find for them.

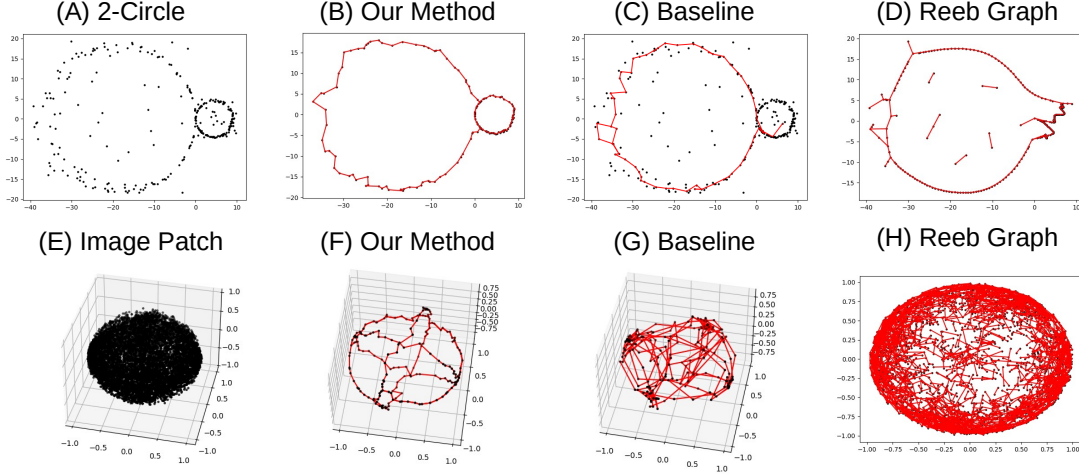


Figure 5: Top row: 2-circle data. Output of our DM-PCD method in (B); of baseline in (C), and of ReebRecon in (D). Using a smaller radius r for baseline and ReebRecon will lose the large circle. Bottom row: image patch dataset with (E) shows projection in \mathbb{R}^3 . For baseline in (G), further simplification will remove the main circle from the “3-circle model” while keeping all the noisy ones. ReebRecon (H) does not work well (too many extra loops), which is expected as there are many background noise, while the method is designed for points within a tubular neighborhood of hidden graph.

More details and additional results (e.g, w.r.t. more parameters for comparison methods) can be found in the appendix.

Synthetic datasets. We create two synthetic PCDs to illustrate the behavior of our DM-PCD algorithm. Circle dataset contains a noisy and non-uniform sample around a hidden circle with 2050 points. See Figure 4: the output of our method (in (C)) recover the hidden circle. In comparison, the output of baseline algorithm over the Rips complex $\text{rips}^r(P)$ at different radius values are shown in (E) – (H). The total number of simplices involved in our sparsified DTM-Rips filtration is 368, 276. The successful baseline result (shown in Figure 4 (G)) however requires 7, 708, 243 simplices, which is about **20 fold** increase in size. In Figure 4 (E), when radius r is chosen so that the size of $\text{rips}^r(P)$ is similar to our sparse DTM-Rips, the underlying shape is not yet captured by $\text{rips}^r(P)$ by baseline. In general, it is not clear which r to choose for baseline, and if r is too large, as shown in Figure 4 (H), then the reconstructed graph is geometrically not faithful any more – this is because long edges are now present in the Rips complex and the DM-graph algorithm may use them. In contrast, our output (in (C)) has lex-optimality (Theorem 3.4) and thus always uses “good” edges (those that enter the filtration early) first. The ReebRecon approach of [24] also uses Rips complex at a fixed scale r and thus has similar issues with baseline; see Figure 4 (I) and (J). The size of complexes involved, as well as the running time of all these algorithms are given in the Supplement. Figure 5 shows the reconstruction from a set of 300 points non-uniformly sampled from two circles (of different sizes) together with background noise. As our algorithm scans through all scales in the filtration, it captures both loop features. In contrast, both baseline and ReebRecon can capture only one of them – using a small radius r , they can capture the small loop but not the big one; to capture the large loop, they need to use a large radius r (as in Figure 5 (C) and (D)), at which point the small loop is destroyed in the Rips complex. See more results on this dataset in the appendix.

Image patches dataset. The image patches dataset from [8] contains 50K points in $\mathbb{S}^7 \subset \mathbb{R}^8$, each of which corresponds to a 3x3 image patch [29]. We subsample 10K points randomly (so that we can experiment with Rips complexes at different radii). See the projection of points in 2D in Figure 5 (E), which is very noisy. However, the analysis of [8] (after denoising) shows that the underlying space has a “three-circle model”, with two circles intersecting the third circle twice but not intersecting each other – so the first Betti number of the underlying space is 5. Our DM-PCD (shown in (F)) successfully recovered the same “three-circle model” (with

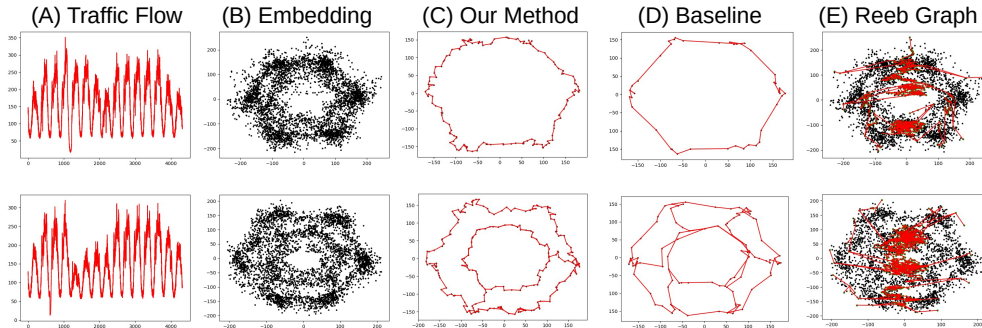


Figure 6: Top row: traffic flow for range (10/1/2017 - 10/14/2017) and bottom row is for range (11/19/2017 - 12/2/2017). (A) input time series, and (B) 2d projections of the time delay embeddings of the time-series. (C) Outputs of our DM-PCD algorithm. (D) Outputs of the **baseline** approach. For the Thanksgiving period, any further simplification will destroy the outer-loop but not those cross connections. (E) Outputs of ReebRecon with $r = 90$ and $r = 75$ respectively. These outputs are noisy, which is not surprising as this method is designed for points within a tubular neighborhood of hidden graph.

correct $\beta_1 = 5$) directly from raw data **without** preprocessing, and the locations of these circles (one outer circle, then a horizontal one and a vertical one) are in the same place as those shown in [8]. Both **baseline** and ReebRecon (in Figure 5 (G) and (H)) fail to capture it. (Refer to the Supplementary Materials for more results.)

Traffic flow dataset. We extract two time-series from pems.dot.ca.gov/?dnode=Clearinghouse, which are the traffic flow at detector #409529 from the time-range 10/1/2017 to 10/14/2017 and from time-range from 11/19/2017 to 12/2/2017 (including Thanksgiving). Each time-series is mapped to a point cloud dataset in \mathbb{R}^6 via time-delay embedding as in [33] (see details in Supplement); their projections in \mathbb{R}^2 are shown in Figure 6 (B). It has been proposed in [33] that loops in the resulting PCD can be used to detect quasi-periodic behavior in the original time-series data. We note that a normal range has one major loop, indicating one major periodicity; while the Thanksgiving period has two: a normal one and another one indicates the traffic pattern for the holidays. Our DM-PCD recovers these much better than **baseline** and ReebRecon. Note that here we use $k = 30$ for both our method and **baseline** as there are local small cluster of points due to the embedding of repeating signals (see Supplement for results from other parameters).

Coil-20 dataset. Finally, we experiment with the **Coil-20** dataset [31], where input points (in \mathbb{R}^{16384}) form loop features across many scales. The analysis of the results is more subtle and can be found in the appendix.

6 Concluding remarks

We generalized the DM-graph reconstruction algorithm to arbitrary filtrations, proved that the output of this generalized algorithm is meaningful, and developed a method for running DM-graph reconstruction on high-dimensional PCDs. Empirical results demonstrate the effectiveness of our DM-PCD approach.

The main limitation of our approach is its time complexity: while the sparsification reduces size, the persistence computation of the sparsified filtration (we use SOA software PHAT [3] to do this) can take cubic time in worst-case (although in practice it is often faster). This is the computational bottleneck; our algorithm takes only linear time after this step. (Note that the **baseline** has the same bottleneck.) It will be interesting to see how this step can be circumvented. We also hope to explore how to extract higher dimensional skeleton for PCDs in the future.

References

- [1] M. Aanjaneya, F. Chazal, D. Chen, M. Glisse, L. Guibas, and D. Morozov. Metric graph reconstruction from noisy data. In *Proc. 27th Sympos. Comput. Geom.*, pages 37–46, 2011.
- [2] S. Banerjee, L. Magee, D. Wang, X. Li, B. Huo, J. Jayakumar, K. Matho, M. Lin, K. Ram, M. Sivaprakasam, J. Huang, Y. Wang, and P. Mitra. Semantic segmentation of microscopic neuroanatomical data by combining topological priors with encoder-decoder deep networks. *Nature Machine Intelligence*, 2:585–594, 2020.
- [3] U. Bauer, M. Kerber, J. Reininghaus, and H. Wagner. Phat – persistent homology algorithms toolbox. In H. Hong and C. Yap, editors, *Mathematical Software – ICMS 2014*, pages 137–143, Berlin, Heidelberg, 2014. Springer Berlin Heidelberg.
- [4] M. Belkin and P. Niyogi. Laplacian eigenmaps for dimensionality reduction and data representation. *Neural Computation*, 15(6):1373–1396, 2003.
- [5] M. Belkin, Q. Que, Y. Wang, and X. Zhou. Toward understanding complex data: graph laplacians on manifolds with singularities and boundaries. In *Conf. Learning Theory (COLT)*, pages 36.1–36.26, 2012. Journal of Machine Learning Research – Proceedings Track 23.
- [6] M. Buchet, F. Chazal, S. Y. Oudot, and D. R. Sheehy. Efficient and robust persistent homology for measures. In *Proceedings of the Twenty-sixth Annual ACM-SIAM Symposium on Discrete Algorithms, SODA ’15*, pages 168–180, Philadelphia, PA, USA, 2015. Society for Industrial and Applied Mathematics.
- [7] C. Cai, N. Vlassis, L. Magee, R. Ma, Z. Xiong, B. Bahmani, T.-F. Wong, Y. Wang, and W. Sun. Equivariant geometric learning for digital rock physics: estimating formation factor and effective permeability tensors from morse graph, 2021.
- [8] G. Carlsson, T. Ishkhanov, V. Silva, and A. Zomorodian. On the local behavior of spaces of natural images. *International Journal of Computer Vision*, 76:1–12, 01 2008.
- [9] F. Chazal, D. Cohen-Steiner, and Q. Mérigot. Geometric inference for probability measures. *Foundations of Computational Mathematics*, 11:733–751, 2011.
- [10] F. Chazal, R. Huang, and J. Sun. Gromov–hausdorff approximation of filamentary structures using reeb-type graphs. *Discrete Comput. Geom.*, 53(3):621–649, Apr. 2015.
- [11] F. Chazal, V. d. Silva, M. Glisse, and S. Oudot. *The structure and stability of persistence modules*. Springer, 2018.
- [12] D. Cohen-Steiner, A. Lieutier, and J. Vuillamy. Lexicographic optimal chains and manifold triangulations, 2019. available at URL: <https://hal.archives-ouvertes.fr/hal-02391190/document>.
- [13] D. Cohen-Steiner, A. Lieutier, and J. Vuillamy. Lexicographic optimal homologous chains and applications to point cloud triangulations. In *36th Sympos. Comput. Geom. (SoCG)*, 2020. to appear, see also url: <https://hal.archives-ouvertes.fr/hal-02391240/document>.
- [14] O. Delgado-Friedrichs, V. Robins, and A. Sheppard. Skeletonization and partitioning of digital images using discrete morse theory. *IEEE Trans. Pattern Anal. Machine Intelligence*, 37(3):654–666, March 2015.
- [15] T. Dey, J. Wang, and Y. Wang. Road network reconstruction from satellite images with machine learning supported by topological methods. In *Proc. 27th ACM SIGSPATIAL Intl. Conf. Adv. Geographic Information Systems (GIS)*, pages 520–523, 2019.
- [16] T. K. Dey, T. Hou, and S. Mandal. Computing minimal persistent cycles: Polynomial and hard cases. In S. Chawla, editor, *Proceedings of the 2020 ACM-SIAM Symposium on Discrete Algorithms, SODA 2020, Salt Lake City, UT, USA, January 5-8, 2020*, pages 2587–2606. SIAM, 2020.

- [17] T. K. Dey, J. Wang, and Y. Wang. Improved road network reconstruction using discrete morse theory. In *Proc. 25th ACM SIGSPATIAL Intl. Conf. Adv. Geographic Information Systems (GIS)*, pages 58:1–58:4, 2017.
- [18] T. K. Dey, J. Wang, and Y. Wang. Graph reconstruction by discrete morse theory. In *Proc. Internat. Sympos. Comput. Geom.*, pages 31:1–31:15, 2018.
- [19] D. Donoho and C. Grimes. Hessian eigenmaps: Locally linear embedding techniques for high-dimensional data. *Proceedings of the National Academy of Sciences*, 100(10):5591–5596, 2003.
- [20] H. Edelsbrunner and J. Harer. *Computational Topology: An Introduction*. Amer. Math. Soc., Providence, Rhode Island, 2010.
- [21] R. Forman. A discrete Morse theory for cell complexes. *Geometry, Topology and Physics for Raoul Bott.*, 1995.
- [22] R. Forman. Combinatorial vector fields and dynamic systems. *Mathematische Zeitschrift*, 228(4):629–681, 1998.
- [23] R. Forman. A user’s guide to discrete Morse theory. *Séminaire Lotharinen de Combinatoire 48*, 2002.
- [24] X. Ge, I. I. Safa, M. Belkin, and Y. Wang. Data skeletonization via reeb graphs. In J. Shawe-Taylor, R. S. Zemel, P. L. Bartlett, F. Pereira, and K. Q. Weinberger, editors, *Advances in Neural Information Processing Systems 24*, pages 837–845. Curran Associates, Inc., 2011.
- [25] A. Gyulassy, M. Duchaineau, V. Natarajan, V. Pascucci, E. Bringa, A. Higginbotham, and B. Hamann. Topologically clean distance fields. *IEEE Trans. Visualization Computer Graphics*, 13(6):1432–1439, Nov 2007.
- [26] T. J. Hastie. *Principal curves and surfaces*. PhD thesis, stanford university, 1984.
- [27] B. Kégl and A. Krzyżak. Piecewise linear skeletonization using principal curves. *IEEE Trans. Pattern Anal. Machine Intell.*, 24:59–74, January 2002.
- [28] F. Lecci, A. Rinaldo, and L. Wasserman. Statistical analysis of metric graph reconstruction. *J. Mach. Learn. Res.*, 15(1):3425–3446, Jan. 2014.
- [29] A. Lee, K. Pedersen, and D. Mumford. The nonlinear statistics of high-contrast patches in natural images. *International Journal of Computer Vision*, 54:83–103, 2004.
- [30] L. McInnes, J. Healy, and J. Melville. Umap: Uniform manifold approximation and projection for dimension reduction, 2020.
- [31] Nayar and H. Murase. Columbia object image library: Coil-100. Technical Report CUCS-006-96, Department of Computer Science, Columbia University, February 1996.
- [32] U. Ozertem and D. Erdogmus. Locally defined principal curves and surfaces. *Journal of Machine Learning Research*, 12:1249–1286, 2011.
- [33] J. A. Perea and J. Harer. Sliding windows and persistence: An application of topological methods to signal analysis. *Found. Comput. Math. (FoCM)*, 15:799–838, 2015. <https://doi.org/10.1007/s10208-014-9206-z>.
- [34] V. Robins, P. J. Wood, and A. P. Sheppard. Theory and algorithms for constructing discrete morse complexes from grayscale digital images. *IEEE Trans. Pattern Anal. Machine Intelligence*, 33(8):1646–1658, Aug 2011.
- [35] S. Roweis and L. Saul. Nonlinear Dimensionality Reduction by Locally Linear Embedding. *Science*, 290(5500):2323, 2000.
- [36] T. Sousbie. The persistent cosmic web and its filamentary structure – i. theory and implementation. *Monthly Notices of the Royal Astronomical Society*, 414:350 – 383, 06 2011.

- [37] J. Tenenbaum, V. Silva, and J. Langford. A Global Geometric Framework for Nonlinear Dimensionality Reduction. *Science*, 290(5500):2319, 2000.
- [38] S. Wang, Y. Wang, and Y. Li. Efficient map reconstruction and augmentation via topological methods. In *Proc. 23rd ACM SIGSPATIAL*, page 25. ACM, 2015.
- [39] P. Wu, C. Chen, Y. Wang, S. Zhang, C. Yuan, Z. Qian, D. N. Metaxas, and L. Axel. Optimal topological cycles and their application in cardiac trabeculae restoration. In *Information Processing in Medical Imaging - 25th International Conference, IPMI 2017, Boone, NC, USA, June 25-30, 2017, Proceedings*, pages 80–92, 2017.

A More details on background and the DM-graph() algorithm

A.1 Simplicial Persistence

Instead of introducing the persistent homology in its full general form, below we focus on the simplicial complex setting. See e.g., [20, 11] for more detailed exposition.

Boundaries, cycles, homology groups. Given a simplicial complex K , let K^q denote the set of q -simplices of K . Under \mathbb{Z}_2 field coefficient (which we use throughout this paper), a q -chain $C = \sum_{\sigma \in K^q} c_\sigma \sigma$ where $c_\sigma \in \{0, 1\}$; equivalently C is a subset of K^q (those with $c_\sigma = 1$). The set of q -chains together with addition operation gives rise to the so-called q -th chain group $C_q(K)$. Given any q simplex σ , its boundary $\partial_q \sigma$ consists of all of its faces of dimension $q-1$. This in turn gives a linear map, called the q -th boundary map $\partial_q : C_q(K) \rightarrow C_{q-1}(K)$, where $\partial_q C = \sum_{\sigma \in K^q} c_\sigma \partial_q(\sigma)$ for any q -chain $C = \sum_{\sigma \in K^q} c_\sigma \sigma$. A q -chain C is a q -cycle if its boundary $\partial_q C = 0$. The collection of all q -cycles form the q -th cycle group Z_q ; that is, $Z_q = \text{kernel } \partial_q$. A q -chain C is a q -boundary if it is the image of some $(q+1)$ -chain C' ; i.e., $C = \partial_{q+1} C'$. The collection of q -boundaries form the q -th boundary group B_q ; that is, $B_q = \text{image } \partial_{q+1}$. By the fundamental property of boundary map, i.e., $\partial_q \circ \partial_{q+1} = 0$, it follows that B_q is a subgroup of Z_q . The q -th homology group H_q is defined as $H_q = Z_q / B_q$. In particular, given any q -cycle C , its homology class $[C]$ is the equivalent class of all q -cycles in $q + B_q(K)$; and two q -cycles C_1, C_2 are homologous if $[C_1] = [C_2]$, implying that $C_1 + C_2$ is a boundary (i.e., $C_1 + C_2 \in B_q(K)$).

Filtration, persistent modules. Suppose we have a finite sequence of simplicial complexes connected by inclusions, called a *filtration of K* , denoted by $\mathcal{F} : K_1 \subseteq K_2 \subseteq \dots \subseteq K_m = K$. Applying the homology functor to this sequence (with \mathbb{Z}_2 coefficients), we obtain a sequence of vector spaces (over field \mathbb{Z}_2) connected by linear maps induced from inclusions, which is called a persistence module; in particular, for any dimension $q \geq 0$, we have:

$$\mathbb{P}\mathcal{F} : H_q(K_1) \rightarrow H_q(K_2) \rightarrow \dots \rightarrow H_q(K_m).$$

where maps are induced by inclusions. In our paper, we assume that the persistence module is indexed by a finite set $[1, m]$ instead of \mathbb{Z} .

A special class of persistence modules is the so-called *interval modules*. (i) $I_i = \mathbb{Z}_2$ for any $i \in [s, t]$ and $I_i = 0$ otherwise; and (ii) $\nu^{i,j}$ is identity map for $s \leq i \leq j \leq t$ and 0 map otherwise. We abuse the notation slightly and allow $t = \infty$, in which case the interval is really $[s, \infty)$. A pictorial version of an interval module is as follows:

$$\dots \rightarrow 0 \rightarrow \mathbb{Z}_2 \rightarrow \mathbb{Z}_2 \rightarrow \dots \mathbb{Z}_2 \rightarrow 0 \rightarrow \dots$$

Persistence diagram. It turns out that a given persistence module \mathbb{V} can be uniquely decomposed into direct sums of interval modules (up to isomorphisms) $\mathbb{V} = \bigoplus_{[b,d] \in J} \mathbb{I}^{[b,d]}$, where J is a multiset of intervals $J = \{[b, d]\}$. We call $\bigoplus_{[b,d] \in J} \mathbb{I}^{[b,d]}$ the interval decomposition of \mathbb{V} . Again, note that the intervals in J could be of two forms: $[b, d]$ for finite $b, d \in \mathbb{Z}$, and $[b, \infty)$; the former is called a *finite interval*. Note that each interval $[b, d]$ can also be viewed as a point in \mathbb{R}^2 . Given a filtration \mathcal{F} , its *persistence diagram* $\text{dgm}\mathcal{F}$ is the multiset of points in J where $\mathbb{P}\mathcal{F} = \bigoplus_{[b,d] \in J} \mathbb{I}^{[b,d]}$ is the interval decomposition of $\mathbb{P}\mathcal{F}$. Each point in J is called a *persistence point*. Assuming that we are given a monotone function $f : \mathbb{Z} \rightarrow \mathbb{R}$, then the persistence

of $\mathbf{p} = [b, d] \in \text{dgm}\mathcal{F}$ w.r.t. f is defined as $\text{pers}(\mathbf{p}) = f(d) - f(b)$ ¹. To make the dependency on the function f explicit, we now write the filtration together with this function as \mathcal{F}_f , and the persistence diagram is denoted by $\text{dgm}\mathcal{F}_f$. For example, a common choice of f in the literature is simply $f(i) = i$.

Simplex-wise setting. In the remainder of this paper, we assume that we are given a *simplex-wise filtration* \mathcal{F} of K , such that there is an ordering of all simplices in K , $\sigma_1, \dots, \sigma_N$, and the filtration is given by:

$$\mathcal{F} : \emptyset = K_0 \subset K_1 \subset \dots \subset K_N = K, \quad \text{where } K_i := \{\sigma_1, \dots, \sigma_i\}. \quad (3)$$

Suppose we are also given a monotone function $\rho : [1, N] \rightarrow \mathbb{R}$ (i.e. $\rho(j) \geq \rho(i)$ for $j > i$), which we use to define the persistence of points in the persistence diagram $\text{dgm}\mathcal{F}_\rho$. (If no function ρ is explicitly given, we take ρ to be $\rho(i) = i$.)

Furthermore, note that for any i , K_i is obtained by adding σ_i to K_{i-1} . Let $\text{ind} : K \rightarrow [1, N]$ be this bijection, where we set $\text{ind}(\sigma_i) = i$. That is, $\text{ind}(\sigma)$ in general is the index of simplex σ in the ordered sequence of simplices that induce simplex-wise filtration \mathcal{F} ; or, the time it will be inserted into a complex (i.e. $K_{\text{ind}(\sigma)}$) in the filtration. Given this bijection, a function on the simplices in K also gives rise to a function on $[1, N]$. In what follows, for convenience, we do not differentiate a function on simplices in K and a function on $[1, N]$; that is, $\rho(\sigma) = \rho(\text{ind}(\sigma))$, and if simplices are ordered as in Eqn (3), then $\rho(\sigma_i) = \rho(i)$. If ρ is defined on simplices in K , we also call it a *simplex-wise function* $\rho : K \rightarrow \mathbb{R}$.

Given any persistence point $[b, d] \in \text{dgm}\mathcal{F}_\rho$ with $b, d \in [1, N]$, we say its corresponding *persistence pair* is (σ_b, σ_d) and it is necessary that $\dim(\sigma_d) = \dim(\sigma_b) + 1$. We set $\text{pers}(\sigma_b) = \text{pers}(\sigma_d) = \text{pers}([b, d]) = \rho(d) - \rho(b)$. If $d = \infty$, then we say σ_b is unpaired, and $\text{pers}(\sigma_b) = \rho(\infty) := \infty$. Finally, consider each persistence pair (σ, τ) , we say that σ is *positive* and τ is *negative*, as the q -simplex σ will create a new homology class that will become trivial (be killed) when the $(q+1)$ -simplex τ is added to the filtration.

A.2 Discrete Morse Theory

Below we very briefly introduce some concepts from discrete Morse theory, so that we can introduce both the original algorithm of [38] (to provide intuition) and the simplified algorithm of [18]. See [22, 23] for more detailed exposition of discrete Morse theory.

We again consider the simplicial complex setting. Given a simplicial complex K , a *discrete gradient vector* is a combinatorial pair of simplices (σ^q, τ^{q+1}) where σ is a face of τ of co-dimension 1 (i.e. σ is a vertex of an edge τ , or an edge of a triangle τ), and we sometimes include the superscript to make its dimension explicit. Given a collection $M(K)$ of such discrete gradient vectors over K , a *V-path* is a sequence of simplices of alternating dimensions: $\sigma_1^q, \tau_1^{q+1}, \dots, \sigma_\ell^q, \tau_\ell^{q+1}, \sigma_{\ell+1}^q$ such that for each $i \in [1, \ell]$, we have (1) $(\sigma_i^q, \tau_i^{q+1}) \in M(K)$ and (2) σ_{i+1}^q is a face of τ_i^{q+1} . We say that a V-path as above is a *non-trivial closed V-path* (or *cyclic*) if $\sigma_1 = \sigma_{\ell+1}$; otherwise, it is *acyclic*.

Definition A.1 (Discrete Morse gradient vector field). *A collection of discrete gradient vectors $M(K)$ of K is a discrete Morse gradient vector field, or DM-vector field for short, if (i) any simplex in K is in at most one vector in $M(K)$; and (ii) no V-path in $M(K)$ is cyclic.*

A simplex in K is critical w.r.t. a DM-vector field $M(K)$ if it does not appear in any gradient vector in $M(K)$.

Now suppose we are given a critical edge e in $M(K)$. The *1-unstable manifold* of e is the union of vertex-edge V-paths $v_1, e_1, \dots, v_\ell, e_\ell, v_{\ell+1}$ such that v_1 is an endpoint of e , while $v_{\ell+1}$ is a critical vertex. Such 1-unstable manifolds correspond to the "valley ridges" in a continuous function $f : \mathbb{R}^d \rightarrow \mathbb{R}$ (the graph of which can be viewed as a terrain), connecting index-1 saddles with minima. They are the opposite of "mountain ridges" (1-stable manifolds), connecting saddles to maxima and separating different valleys.

Finally, we note that there is a *Morse cancellation* operation that allows one to cancel a pair of critical simplices, and thus reduce both the number of critical simplices as well as the complexity of 1-(un)stable manifolds. In particular, a pair of critical simplices $\langle \sigma^q, \tau^{q+1} \rangle$ is *cancellable* if there is a unique V-path $\sigma_1, \tau_1, \dots, \sigma_\ell, \tau_\ell, \sigma_{\ell+1} = \sigma^q$ in $M(K)$ such that σ_1 is a face of τ^{q+1} . The Morse cancellation operation will essentially invert the gradient vectors along this V-path and render σ^q and τ^{q+1} no longer critical afterwards:

¹We note that in the literature, the persistence of a pair is often defined using some indices (\mathbb{Z} or \mathbb{R}) of the filtration. Here we decouple the two to make the presentation cleaner.

A.3 Discrete Morse based Graph Reconstruction

In what follows, we first state the original persistence-guided discrete Morse based algorithm, called `firstDM-graph()`, from [38], which follows a similar idea as [36]. We use this algorithm to provide intuition as to why this could reconstruct a hidden graph. We then present the simplified algorithm from [18], called `DM-graph()`, which we generalize in Section 3 of the main paper.

Intuition behind Algorithm `firstDM-graph()` of [38]. We briefly describe the intuition behind algorithm `firstDM-graph(K, ρ, δ)`. First, consider the continuous case where we have a density $\rho : \mathbb{R}^d \rightarrow \mathbb{R}$. If we view the graph of this density function as a terrain in \mathbb{R}^{d+1} (see Figure 1 (B) of main paper), then its graph skeleton can be captured by the “mountain ridges” of this density terrain, as intuitively, the density on such ridges is higher than the density off the ridges. To simplify the terrain and only capture “important” mountain ridges, we use persistent homology, and simplify those pairs of critical points with persistence of at most δ .

In the discrete setting imagine K is the 2-skeleton of a domain Ω of interest, ρ is a density function defined on Ω but is only accessible at vertices $V(K)$ of K , i.e., $\rho : V(K) \rightarrow \mathbb{R}$. Algorithm `firstDM-graph($K, \rho : V(K) \rightarrow \mathbb{R}, \delta$)` will output a graph consisting of edges of K capturing a graph skeleton of the density field ρ by the following three steps:

- (Step 1): Compute persistence pairing \mathcal{P} induced by the lower-star filtration w.r.t. $-\rho$.

Specifically, we use $f = -\rho$ as it is easier to algorithmically compute the discrete analog of “valley ridges” using discrete Morse theory than “mountain ridges” – The valley ridges are the 1-unstable manifolds (vertex-edge V-paths) for critical edges, and thus only 2-skeleton of input complex K is needed. To compute the importance of critical points in the simplicial setting when we are given $f : V(K) \rightarrow \mathbb{R}$, we use the standard lower-star filtration to simulate the so-called sublevel-set filtration in the smooth case. In particular, given $f : V(K) \rightarrow \mathbb{R}$, let $v_1 \dots v_n$ be the set of vertices in K sorted in non-decreasing order of f values. Given any vertex $v_i \in V(K)$, its *lower-star* $\text{lowSt}(v_i)$ consists of the set of simplices incident on v_i spanned by only vertices from $V_i := \{v_1, \dots, v_i\}$. The lower-star filtration w.r.t. f is the following:

$$\widehat{K}_1 \subset \widehat{K}_2 \subset \dots \widehat{K}_n = K; \quad \text{where } K_i = K_{i-1} \cup \text{lowSt}(v_i). \quad (4)$$

Equivalently, we can think that this filtration is induced by a simplex-wise function $\hat{f} : K \rightarrow \mathbb{R}$ where $\hat{f}(\sigma) = \max_{\text{vertex } v \text{ of } \sigma} f(v)$.

- (Step 2): Initialize vector field $M(K)$ to be the trivial one where all simplices are critical. Then in order of increasing persistence, for each pair $(\sigma, \tau) \in \mathcal{P}$ with $\text{pers}(\sigma, \tau) \leq \delta$, perform discrete Morse cancellation and update $M(K)$ if possible. Intuitively, this is to simplify and remove “not-important” critical points.
- (Step 3): Output the graph $G_\delta = \bigcup_{e \in K, \text{pers}(e) > \delta} \{ \text{1-unstable manifold of } e \}$.

In particular, we only consider critical edges that are “important” (i.e., $\text{pers} > \delta$). Then we trace the valley ridges (1-unstable manifolds) connecting them to minima.

Simplified algorithm. It turns out that algorithm `firstDM-graph()` can be significantly simplified [18]. In particular, one does not need to explicitly maintain any discrete Morse gradient vector field at all. See Algorithm `DM-graph()` below.

In particular, in (Step 3) above, we only consider critical edges with $\text{pers} > \delta$, and their 1-unstable manifolds turn out to be the union of tree paths as specified in Eqn (5). Note that (Step 2, 3) can be implemented in time linear to the number of vertices and edges in K .

B Further study of alternative approaches

Different input triangulations for baseline Our main experiments compare the quality of our DM-PCD method to the baseline algorithm. `baseline` takes an input triangulation, for which we chose the Rips complex at a fixed radius. We tested other input triangulations to highlight that the baseline approach fails regardless

Algorithm 3: DM-graph(K, ρ, δ)

Input: Triangulation K , density function $\rho : V(K) \rightarrow \mathbb{R}$, persistence threshold δ

Output: a graph skeleton G_δ

(Step 1) Compute persistence pairing \mathcal{P} induced by the lower star filtration w.r.t. $-\rho$,

(Step 2) Set $\mathcal{T}_\delta := \{e \in E \mid e \text{ is negative and } \text{pers}(e) \leq \delta\}$

For each component (tree) T in \mathcal{T}_δ , set its root to be $r(T) := \text{argmin}_{v \in T} \rho(v)$.

(Step 3) Let $\pi_T(x, y)$ be the tree path from x to y in a tree T . Output:

$$G_\delta = \bigcup_{e=(u,v), \text{pers}(e) > \delta} \{e \cup \pi_{T_{i_1}}(v, r(T_{i_1})) \cup \pi_{T_{i_2}}(u, r(T_{i_2})) \mid u \in T_{i_1}, v \in T_{i_2} \text{ in } \mathcal{T}_\delta\}. \quad (5)$$

of the input triangulation. Results are showing in Figure 7. Even using sparse weighted Rips complex at a fixed radius large enough to capture the larger feature with less noise compared to a regular Rips complex, the points forming the smaller feature are connected by nearly a clique. Using this triangulation with any valid density function into the baseline algorithm results in the smaller feature being lost. It is also shown that using the weighted Rips complex without sparsification results in a similar triangulation and final output.

Different input filtrations for generalized algorithm Our DM-PCD algorithm takes a sparse weighted Rips filtration of a point cloud dataset. However, we generalized the discrete Morse graph reconstruction algorithm to take an arbitrary filtration. To highlight the utility of the sparse weighted Rips filtration, we run the generalized discrete Morse graph reconstruction algorithm with both the regular Rips filtration and the regular weighted Rips filtration. Results are shown in Figure 8. Using the regular Rips filtration, the output captures the two features with a lot of additional noise. Trying to use persistence thresholding to remove the noise will remove the smaller feature before all noise is removed. The regular weighted Rips filtration is able to perfectly capture both features, similarly to using the sparse weighted Rips filtration. However, because the persistence computation of the filtration is a bottleneck, the sparse filtration is a superior option for our DM-PCD algorithm.

Dimensionality reduction of noisy data

For noisy datasets, such as the image patches dataset, dimensionality reduction techniques fail to reveal meaningful structure. PCA (A), tSNE (B), and UMAP (C) projections of 10,000 image patches subset are shown in Figure 9. While our DM-PCD algorithm extracts a clear three circle structure that is known to be the true underlying shape of the data, none of the projections come close to revealing any meaningful structure. On a whole, this is because these methods do not look to preserve metric relations. In particular, tSNE attempts to cluster data and UMAP attempts to preserve continuous structure. For cleaner datasets, such as Coil-20 (D), we see that UMAP is able to capture structure (we further examine the Coil-20 dataset in Section C. However, even applying PCA (E) and UMAP (F) to the much cleaner $X(15, 30)$ subset of image patches, we see that UMAP is unable to capture the known three circle structure of the data.

C More details on experiments

Comparison of methods Our experiments compare the quality of outputs and computational efficiency of our DM-PCD method with both the baseline algorithm and the state-of-the-art ReebRecon algorithm.

The ReebRecon algorithm has two outputs - a contracted output, which contains non-degree two nodes, and an augmented output, which contains edges going through every possible node in the domain. While the contracted outputs are useful for examining the topology of the output, they do a poor job of preserving the underlying geometry of the output. On the other hand, the augmented outputs are very noisy because every node is included. For this reason, the authors of the ReebRecon algorithm smooth outputs. We smooth the augmented outputs by subsampling the arcs (non-degree two paths), and then perform standard iterative smoothing on the remaining vertices. An example is shown in Figure 10. Unless otherwise noted, the ReebRecon results displayed in figures are the smoothed augmented outputs. Ultimately, the quality of the output is now dependant on the smoothing, and we note that different smoothing techniques may result

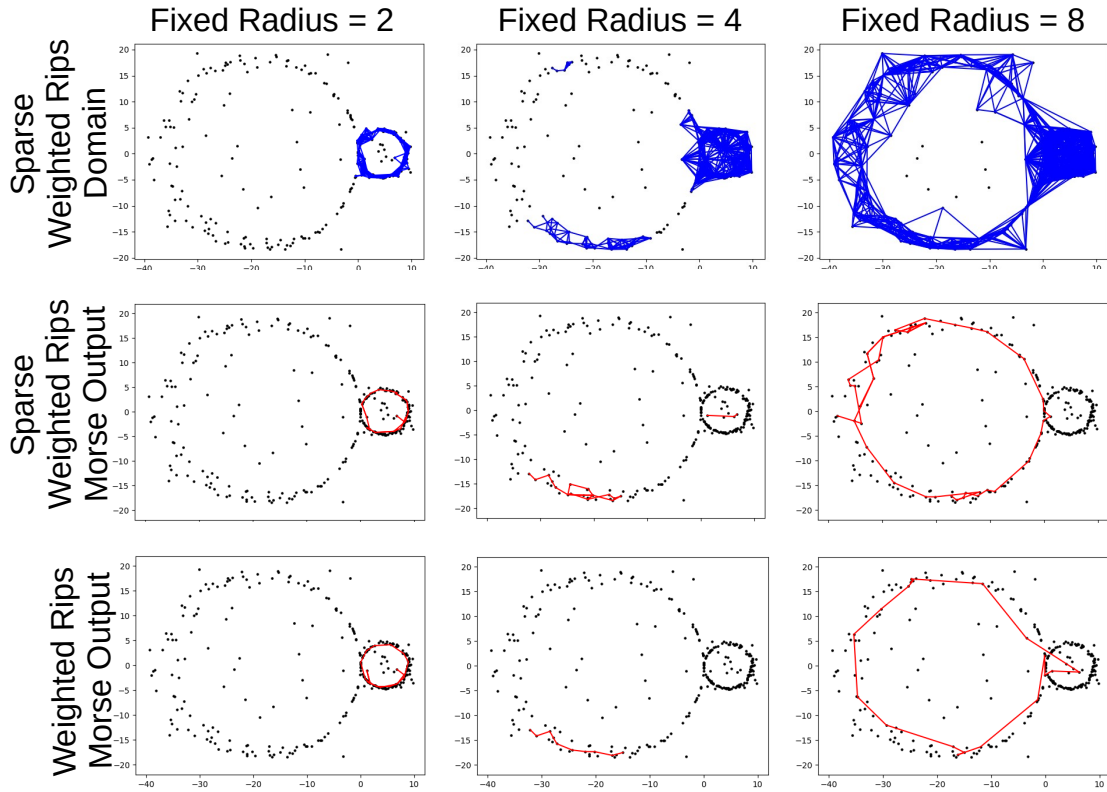


Figure 7: Sparse weighted Rips complex at fixed radii (first row) with results of baseline using sparse weighted Rips complex (second row) and full weighted Rips complex (third row). Fixed radii values of 2 (first column), 4 (second column), and 8 (third column) are shown.

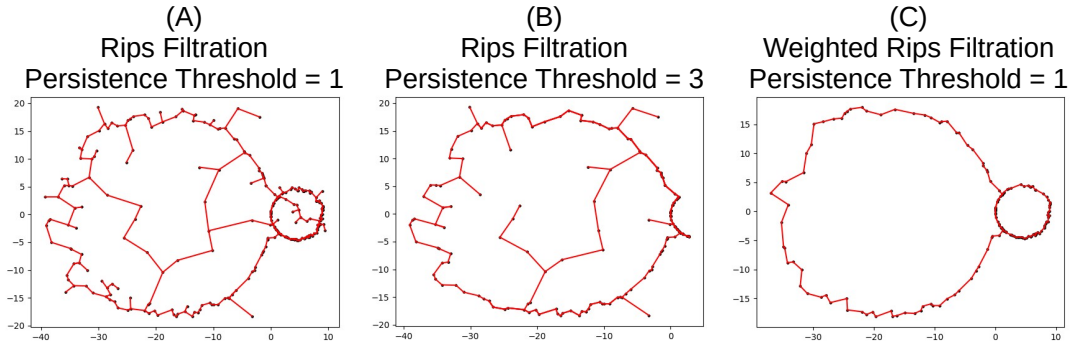


Figure 8: Results of using the generalized discrete Morse algorithm with the regular Rips filtration as input. At a lower persistence threshold (A), both features are captured with additional noise. At a higher persistence threshold (B), the smaller features is lost while some noise remains. Using the weighted Rips filtration as input (C), the algorithm is able to recover both features with no noise.

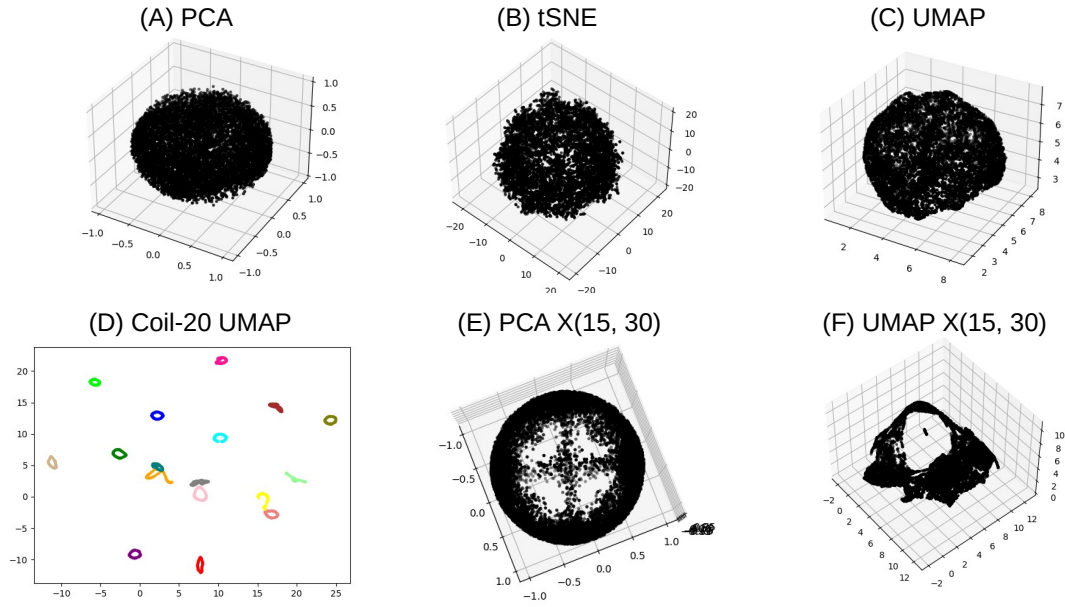


Figure 9: Outputs of various dimensionality reduction techniques (PCA, tSNE, and UMAP) performed on the 10,000 image patch subset, Coil-20, and $X(15, 30)$.

in better quality outputs. However, the topology of the outputs is often incorrect, and in such cases no smoothing can make the output "correct".

In our time comparisons, ReebRecon is much slower than both DM-PCD and baseline. While we are using an old implementation from 2011 that may not be optimized, it is known that ReebRecon is theoretically faster than both DM-PCD and baseline, which have persistence computation as a bottleneck. DM-PCD tends to be more efficient than baseline, as the sparsification in our algorithm builds a filtration that is linear in size with respect to the number of points, whereas the regular Rips complex used in baseline results in a filtration of size $O(n^2)$, and r values large enough to capture the underlying skeleton will have much bigger filtrations.

One Circle dataset.

The main paper shows that our DM-PCD algorithm is able to successfully capture the circle, and both the baseline and ReebRecon capture the circle with $r = .25$. However, the quality of output for both baseline and ReebRecon is heavily dependent on the value of r - more specifically the corresponding $\text{rips}^r(P)$ complex. Shown in the first row of Figure 11 is the $\text{rips}^r(P)$ complex for r values of .1 (A), .2 (B), .25 (C), and 1.05 (D).

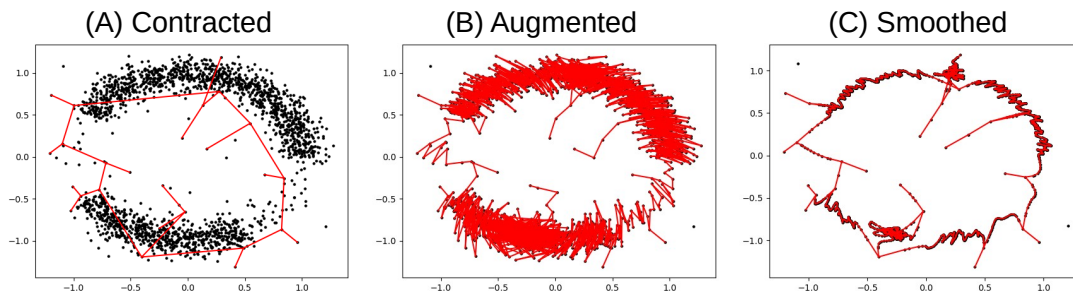


Figure 10: The contracted output (A) and the augmented output (B) of the ReebRecon algorithm with $r = .25$. The contracted output is useful in examining the topology of the output, but does a poor job of preserving the geometry of the underlying skeleton. The augmented output better preserves the geometry but contains a lot of noise. (C) is a smoothed augmented output with less noise.

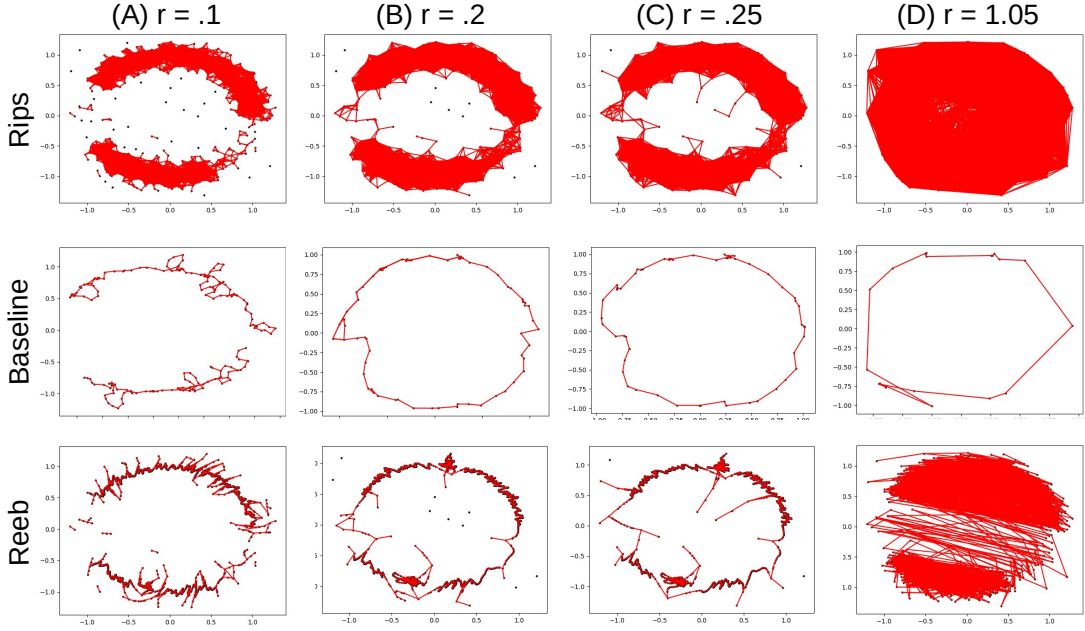


Figure 11: The $\text{rips}^r(P)$ complex (first row), baseline outputs (second row), and ReebRecon outputs (third row). (A) $r = .1$ - $\text{rips}^r(P)$ complex fails to capture the circle, resulting in both methods failing to capture the circle. (B) $r = .2$ - $\text{rips}^r(P)$ complex now contains the circle, but also contains a spurious loop. Both the baseline output, which was generated with persistence threshold $\delta = \infty$, and the ReebRecon output must contain this spurious loop (C) $r = .25$ - $\text{rips}^r(P)$ complex now contains the circle without any additional spurious loops. Both the baseline output ($\delta = \infty$) and the ReebRecon output capture the loop. (D) $r = 1.05$ - $\text{rips}^r(P)$ complex still contains the circle, as well as many more simplices. As a result, the baseline output has lost its nice geometry, with long edges going through high density regions, and the ReebRecon output is a spanning tree.

The second and third rows contain results of baseline and ReebRecon. All ReebRecon outputs are smoothed with no subsampling, a neighborhood radius of 2 neighbors, and 5 iterations - except for (D), where the output is a spanning tree and smoothing does not improve output quality. With an r value too small (.1), the underlying skeleton is not contained in $\text{rips}^r(P)$, and neither method will be able to produce a desirable output. It is not enough to select an r value that results in the complex containing the underlying skeleton. For $r = .2$, the circle is captured by the $\text{rips}^r(P)$ complex, but so is an additional spurious loop. Neither baseline or ReebRecon can produce an output not containing the spurious loop. For $r = 1.05$, there are no additional spurious loops in the $\text{rips}^r(P)$ complex, but ReebRecon produces a spanning tree and baseline, while producing a single loop, loses the geometry of the underlying skeleton.

For this dataset, $r = .25$ was an appropriate selection for both baseline and ReebRecon. However, as shown in Table 1, the size of the $\text{rips}^r(P)$ complex is much bigger than the sparsified weighted Rips complex used in our DM-PCD algorithm. Complex size is particularly costly for our DM-PCD method and the baseline method because of the persistence computation. While baseline was able to produce a reasonable output at $r = .25$, it took significantly more time than our DM-PCD algorithm.

While smoothing certainly decreases the noise in the ReebRecon output, the output quality is still worse than that of both DM-PCD and baseline. We comment that a different smoothing method may result in a better quality output.

Two Circle dataset. The main paper shows that our DM-PCD algorithm is able to successfully capture both circles, while both baseline and ReebRecon failed to capture both circles. Again, this is because both methods are heavily dependent on the input triangulation (the $\text{rips}^r(P)$ complex). This complex at various values of r is shown in the first row of Figure 12, while the corresponding baseline and ReebRecon outputs are shown in the second and third rows respectively. All ReebRecon outputs are smoothed with no subsampling, a neighborhood radius of 2 neighbors, and 10 iterations. Neither result can contain the larger circle if the input

Method	Radius	# Simplices	Time (seconds)
Our Method	∞	368276	2.6
Baseline	.05	33368	.1
Reeb Graph	.05	33368	.03
Baseline	.10	356925	1.1
Reeb Graph	.10	356925	2.49
Baseline	.15	1490149	5.4
Reeb Graph	.15	1490149	21.05
Baseline	.2	3869507	13.0
Reeb Graph	.2	3869507	76.46
Baseline	.25	7708243	44.8
Reeb Graph	.25	7708243	221.25
Baseline	.5	43392850	231.1
Reeb Graph	.5	43392850	3445.10

Table 1: Circle dataset: comparison of radius used, # simplices, and running time of DM-PCD, baseline, and ReebRecon. Our algorithm has radius ∞ as we run on the full sparse DTM-Rips filtration.

triangulation itself does not contain the larger circle, so we increase values of r until the complex contains the larger circle. $r = 1$ is too small to capture even the smaller circle. At $r = 1.5$, the complex does contain the smaller circle, and both baseline and ReebRecon are able to successfully extract the loop. However, at $r = 2$ and $r = 3$, the complex still does not contain the larger circle, and more noise around the smaller circle is added to the outputs. Finally, at $r = 4$, the larger circle is contained within the complex. However there are two issues. Firstly, there is a spurious loop in the complex along the larger circle, so while $r = 4$ is able to capture the larger circle, it is still not an appropriate value of r . We would need to try to find a new r value that better captures the data if not for the second issue - the smaller circle is lost in both outputs - making an appropriate r -value not possible for either method. We can see that in the $\text{rips}^r(P)$ complex at $r = 4$, the points forming the smaller circle now nearly form a clique, which results in both baseline and ReebRecon outputs losing the smaller circle. We conclude that there is no value for r that will result in either method capturing both circles.

We note that the runtime for persistence in DM-PCD was .06 seconds (19,497 simplices), the runtime for persistence in baseline was ($r = 4$) .13 seconds (41,349 simplices), and the runtime for ReebRecon ($r = 4$) was .25 seconds.

Image patches dataset.

The main paper shows that our DM-PCD algorithm is able to successfully extract the "three-circle model" from a random 10,000 point subset of the image patches dataset from [8], while both baseline and ReebRecon methods are unable to do so. We run baseline with $\text{rips}^{.75}(P)$ as the input complex. We tried several r values less than .75, as well as $r = .8$. For r values less than .75, there were many spurious loops that could not be removed with persistence thresholding. For $r = .8$, the desired three-circles are not completely recovered even with no persistence thresholding. Results at various persistence thresholds are shown in Figure 13. Although the output does contain the three circles we wish to extract, it is also made up of several additional loops. Raising the persistence threshold to 5 removes some of the additional loops, but raising the persistence threshold to 10 removes part of the desired three circle model without removing the remaining additional loops. In fact, raising the persistence threshold to ∞ , we see that some of these incorrect loops are a product of the input triangulation, and it is not possible to achieve a desired output from baseline with $r = .75$. While it may still be possible for a "good" r value to exist, it is extremely expensive to compute persistence on triangulations with this many simplices.

The ReebRecon output shown in the main paper takes $r = .25$ as input. The three circle model shape is visible in the output, but the topology of the output is far from that of the three circle model. Relevant topological information for ReebRecon at various r values is shown in Table 2. The table contains the number of simplices in the $\text{rips}^r(P)$ complex, as well as the number of connected components and the first betti number of the output. Despite appearing to resemble the three-circle-model, the ReebRecon output with $r = .25$ has 452 connected components and a first betti number of 629! This output is not close to the true

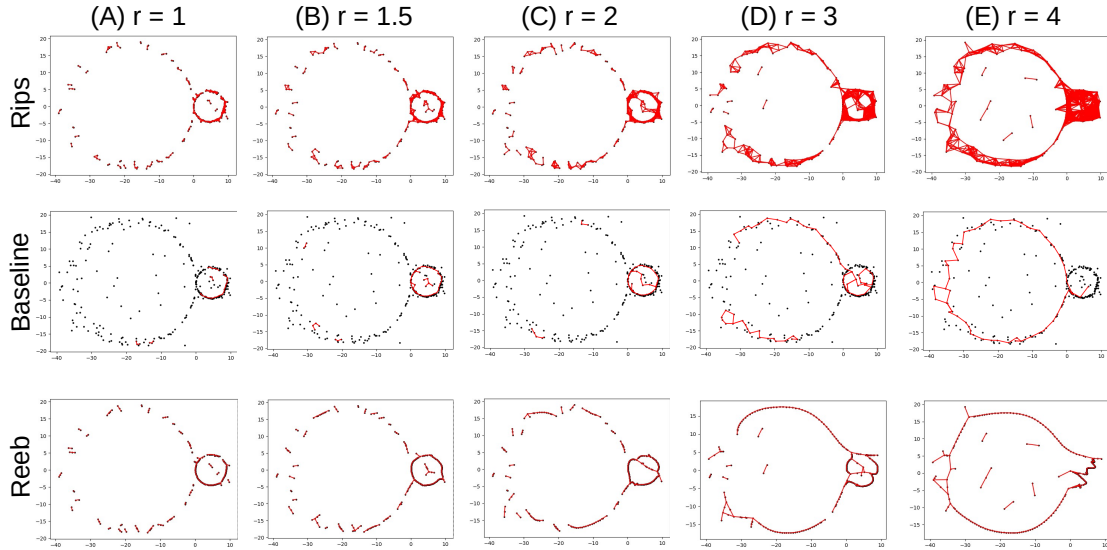


Figure 12: The $\text{rips}^r(P)$ complex (first row), **baseline** outputs (second row), and **ReebRecon** outputs (third row). All **baseline** outputs were generated using persistence threshold zero, meaning that no simplification occurred. (A) $r = 1$ - $\text{rips}^r(P)$ complex fails to capture either circle, resulting in both methods failing to capture either circle. (B) $r = 1.5$ - $\text{rips}^r(P)$ complex now contains the smaller circle but not the larger circle. Both outputs successfully capture the smaller circle, but fail to capture the larger circle. (C) $r = 2$ - $\text{rips}^r(P)$ complex now connects the noise inside of the smaller circle to the smaller circle, while still not containing the larger circle. The outputs now capture the smaller circle and some noise inside of the circle, and still fail to capture the larger circle. (D) $r = 3$ - $\text{rips}^r(P)$ complex still does not contain the larger circle, and contains many edges cutting across the smaller circle. The **ReebRecon** output captures the smaller circle with more noise, while the **baseline** output has begun to lose the smaller circle. Both outputs fail to capture the larger circle. (E) $r = 4$ - $\text{rips}^r(P)$ complex now contains the larger circle, as well as a spurious loop, and the points forming the smaller circle now nearly form a clique. The outputs capture the larger circle, but contain a spurious loop, and the smaller circle is completely lost.

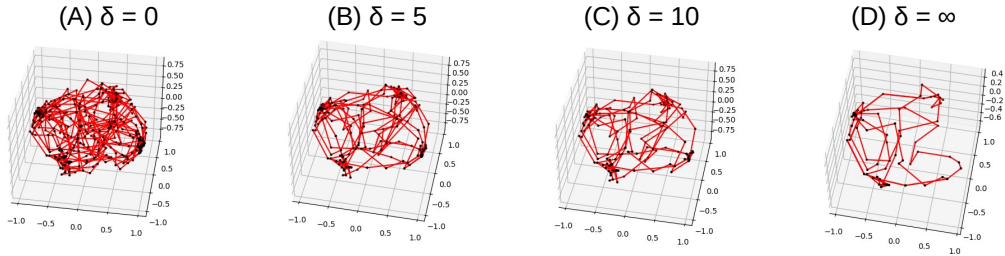


Figure 13: Outputs of baseline with $\text{rips}^r(P)$ complex ($r = .75$) as the input triangulation at various persistence thresholds. (A) $\delta = 0$ - With no thresholding of critical edges, the output captures the three circles that we expect to, as well as additional loops. (B) $\delta = 5$ - Raising the persistence threshold allows for some of the additional loops to be removed while keeping the three circles we expect. (C) $\delta = 10$ - Further raising the persistence threshold results in losing part of the horizontal circle while keeping extra loops. (D) $\delta = \infty$ - Removing all critical edges except those with infinity persistence removes more of the desired three circle output and keeps loops not part of the desired output.

underlying skeleton. We see that at $r = .75$ the connected components and first betti number appear much closer to those of the desired output, but the geometry of the output is not correct.

We note that the runtime for persistence in DM-PCD was 16089.4 seconds (209,397,755 simplices), the runtime for persistence in baseline was ($r = .75$) 1485.42 seconds (263,787,145 simplices), and the runtime for ReebRecon ($r = .75$) was 25447.76 seconds.

Rips Radius	# Simplices	# Components	First Betti Number
.25	79,416	452	629
.35	841,893	275	1,167
.45	5,698,454	63	1,539
.55	26,090,870	1	998
.65	91,456,427	1	271
.75	263,787,151	1	6

Table 2: Image Patches dataset: comparison of radius used, # simplices in corresponding Rips complex, and # of components and first Betti number in contracted ReebRecon output.

Traffic flow dataset.

We also test on point clouds derived from traffic flow data (<https://pems.dot.ca.gov/?dnode=Clearinghouse>). We extract two datasets: the time-series of traffic flow at detector #409529 from time-range 10/1/2017 to 10/14/2017 and from time-range 11/19/2017 to 12/2/2017 (which includes Thanksgiving). Each time-series is mapped to a point cloud dataset in \mathbb{R}^6 via time-delay embedding.

Given a time series $f : t \rightarrow \mathbb{R}$ and a parameter τ , the lift defined by $\phi(t) = (f(t), f(t+\tau), \dots, f(t+M\tau))$ is called a time delay embedding. For each traffic flow function, we create a PCD using a time delay embedding with $M = 5$ and $\tau = 50$. The two dimensional projections of these PCDs are shown in Figure 4 (B) of the main paper. The first function’s time delay embedding projection appears to be a single loop, while the second appears to have an inner loop and an outer loop.

The main paper shows the results of our DM-PCD algorithm with $k = 30$ on both time series datasets. So far in our experiments, a default value of $k = 15$ has been used. By the nature of time delay embeddings, which may create clumps of points close together, different values of k can produce markedly different results. Shown in Figure 14 are results of DM-PCD on the two datasets with k values of 15, 30, and 40. For the first dataset (10/1/2017 - 10/14/2017), a single loop is captured with all values of k . For the second dataset (11/19/2017 - 12/2/2017), changing the value of k results in more drastic changes in the output. The persistence thresholds for the outputs are 8.25 ($k = 15$), 12.5 ($k = 30$), and 12.84 ($k = 40$). In all cases, if the persistence threshold were raised enough to further threshold the output, a portion of the outer loop would be lost. We note that our output must be connected, so the desired result is two loops with a single connection. The output with $k = 15$ contains many extra connections, while the output with $k = 30$ contains

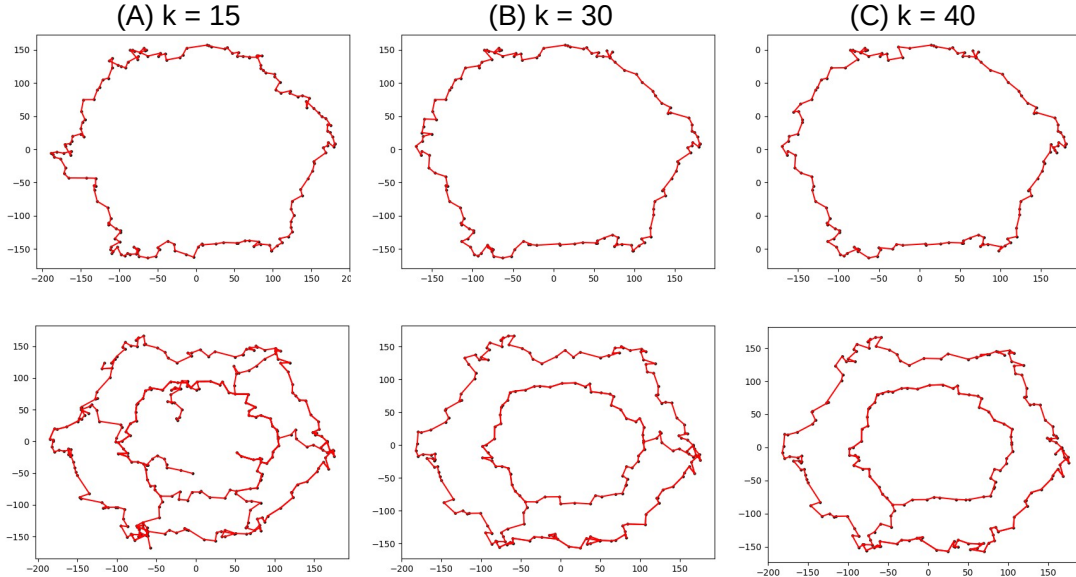


Figure 14: Outputs of DM-PCD on both traffic time series datasets (10/1/2017 - 10/14/2017 top row, 11/19/2017 - 12/2/2017 bottom row) with different values of k . (A) $k = 15$ - Single loop captured in first dataset, two loops captured with extra connections in second dataset. (B) $k = 30$ - Single loop captured in first dataset, two loops captured with an extra connection in second dataset. (C) $k = 40$ - Single loop captured in first dataset, two loops captured with a single connection in second dataset.

a single extra connection. With $k = 40$, the desired output is achieved.

Also shown in the main paper, **baseline** is able to successfully capture the single loop of the first time series dataset. Results for **baseline** on the second time series dataset are shown in Figure 15. The persistence thresholds for the outputs are 8 ($k = 15$), 5 ($k = 30$), and 3 ($k = 40$). Just like the results for DM-PCD in Figure 14, if the persistence thresholds were raised enough to further threshold the output, a portion of the outer loop would be lost, making the output of DM-PCD superior.

We do not show more ReebRecon outputs because despite differences in topology, results look largely the same as the one shown in the main paper despite smoothing, and we could not obtain a reasonable output.

We note that the runtime for persistence in DM-PCD was 98.6198 seconds (6879338 simplices) and the runtime for persistence in **baseline** ($r = 90$, 10/1/2017 - 10/14/2017 dataset) was 123.903 seconds (35543784 simplices).

Coil-20.

In our final experiment, we use the Coil-20 dataset provided by [31]. More specifically, we take a subset of 17 objects - removing objects 5, 6, and 19. Objects 5 and 9 are both medicine boxes, and objects 3, 6, and 19 are toy cars, and we wanted to evaluate our method’s performance on a dataset containing unique objects. We refer to this subset as Coil-17. Following the process used by [30] to convert images to point clouds, we convert each 128 x 128 gray scale image into a 16384 dimensional vector. Hence the input is a set of 1224 points in \mathbb{R}^{16384} .

We visualize the data in two dimensions using UMAP dimensionality reduction with L1 metric. Presumably, each class forms a high-dimensional loopy shape. We run DM-PCD using L1 metric with $k = 5$. Shown in Figure 16 is the UMAP reduction with objects uniquely colored (A), the output of our DM-PCD algorithm with a persistence threshold of 0 (B), the output of our DM-PCD algorithm with a persistence threshold of 56 (C), and the output in (C) after removing the critical edges with L1 length above a threshold of 1700 in the 16384 dimensional original space (D). The raw output contains the loops that we would expect to see based on our understanding of our data and the shapes formed in the UMAP projection. The raw output also contains many other edges, revealing more relationships within individual classes and between classes in the feature space. We remove the longer edges in order to better highlight the features of the output that

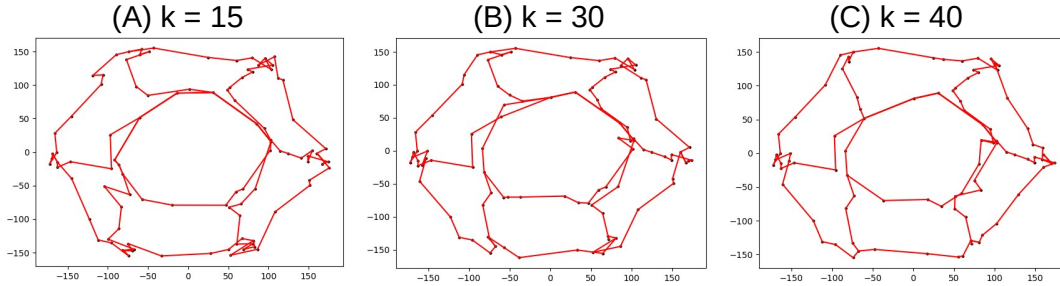


Figure 15: Outputs of baseline method on the second traffic time series dataset (11/19/2017 - 12/2/2017) at different values of k - (A) $k = 15$, (B) $k = 30$, (C) $k = 40$. In all cases, any further simplification will lose the outer loop before removing any connections with the inner loop.

capture individual objects.

Taking a closer look at Figure 16 (D), there are eight objects that the DM-PCD captures in the same exact manner that the UMAP projection does. Close up pictures of these eight objects are shown in Figure 17.

There are also four objects that both the DM-PCD output and the UMAP projection capture as loops, but the loops differ between the two. Close up pictures of these four objects are shown in Figure 18. Object 11 (A) is a single loop in the UMAP projection, but is actually two full loops in the DM-PCD output. A closer look (B) at images 16, 17, 54, and 55 shows two separate loops in the output. The L1 distances between these images in the 16384 dimensional original space (1069.2157046029981, 1038.6980409049952, 693.1607849029981, and 566.901973108997) for pairs (16,54), (17,55), (16,17), and (54,55) respectively) does not match the distances between the pairs in the UMAP projections. This indicates that the UMAP projection does not preserve the underlying structure of this object, and that the DM-PCD output containing two loops is correct.

A similar result is obtained for Object 14 (C), where UMAP projects a single loop and the DM-PCD contains multiple loops. Objects 11 and 14 are symmetrical, adding further justification that multiple loops is a better skeletonization.

Object 2 (D) makes a complete loop in the DM-PCD output, but the loop looks incomplete in the UMAP projection. We ran UMAP projections on smaller subsets of Coil-20, some of which project Object 2 as a clear loop (E), whereas the DM-PCD output consistently captures Object 2 as a loop.

Object 20 (F) is captured as the same loop in both the UMAP projection and the DM-PCD output, but the DM-PCD has an additional edge dividing the loop. The edge connects images 44 and 70, which have a L1 distance of 1329.8000237339966 in the original space. While the other edges adjacent to these nodes are much shorter, other edges that would similarly divide the loop into two are much longer. For example, the L1 distance between images 19 and 58 is 1822.1608110429997. The dividing edge in the DM-PCD output captures this difference, whereas the UMAP projection has no indication of such a difference.

For the remaining five objects, it is not as clear whether or not the DM-PCD output is correct. Close ups of all five objects are shown in Figure 19. For each object, the figure shows the output at persistence thresholds $\delta = 0$ (first row), $\delta = 56$ (second row), and $\delta = 56$ with critical edges longer than 1700 removed (third row). Object 3 (A) and Object 18 (E) are not captured as a loop in either the UMAP projection or in any DM-PCD output. The arcs appear to follow the arcs embedded in the UMAP projection. Object 9 (B) does appear as a loop in the UMAP projection, but is captured as a (double) arc by DM-PCD. Object 12 (C) is captured as a loop in UMAP, but is not in any DM-PCD output. However an arc spanning most of the loop is clearly captured. Under different parameters, DM-PCD was able to extract a loop. Object 16 (D) is captured as a loop in UMAP, and a loop is only captured by DM-PCD output with persistence threshold $\delta = 0$.

A final note on comparing DM-PCD to UMAP projections is that the metric distortion of UMAP became apparent when viewing the DM-PCD outputs. There was metric distortion within classes - such as Object 20, where there appears to be an extra edge in the DM-PCD because the UMAP embedding does not preserve the distances in the original space. There is also clear metric distortion in the UMAP embedding with respect to object relations. For example, before removing critical edges with length greater than 1700, both Objects 4 and 16 have an edge that connects to Object 8. However, once the thresholding is applied, the edge connecting

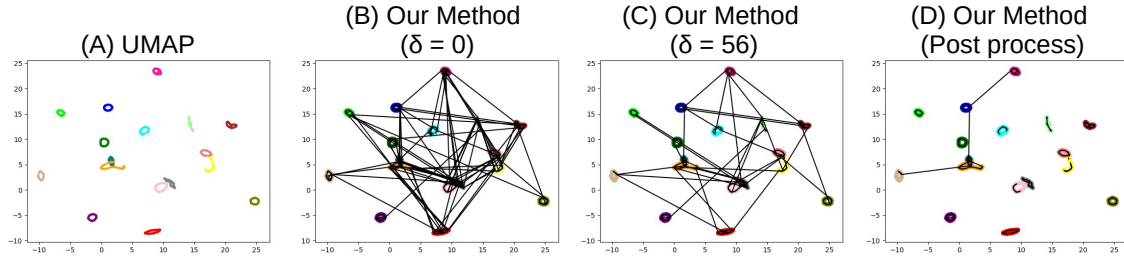


Figure 16: (A) The UMAP projection (using L1 metric) of Coil-17. (B) Output of our DM-PCD algorithm with persistence threshold $\delta = 0$. (C) Output of our DM-PCD algorithm with persistence threshold $\delta = 56$. (D) The output shown in (C) with critical edges of L1 length greater than 1700 removed from the output.

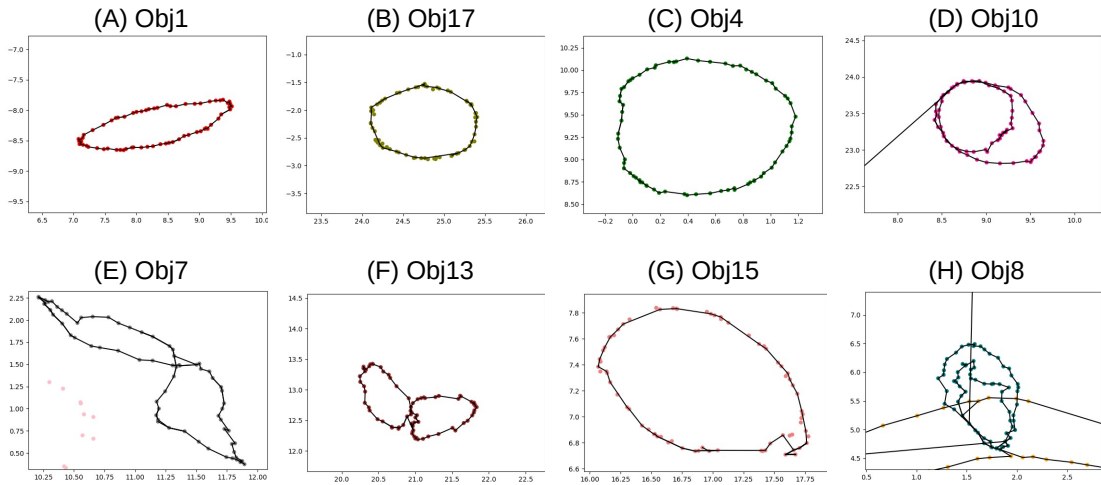


Figure 17: Zoom ins of Figure 16 (D) on the eight objects for which our DM-PCD post processed output matches the UMAP projection.

Objects 4 and 8 is removed and the edge connecting Objects 16 and 8 remains. This would indicate that Object 16 is closer to Object 8 than Object 4 is, but Object 4 appears closer in the UMAP embedding.

Similarly to the two circle example, both the baseline and ReebRecon approaches are unable to capture all coils because the coils have varying scales in the original space. A concrete example is shown in Figure 20, where Objects 1 and 17 cannot be captured at the same scale.

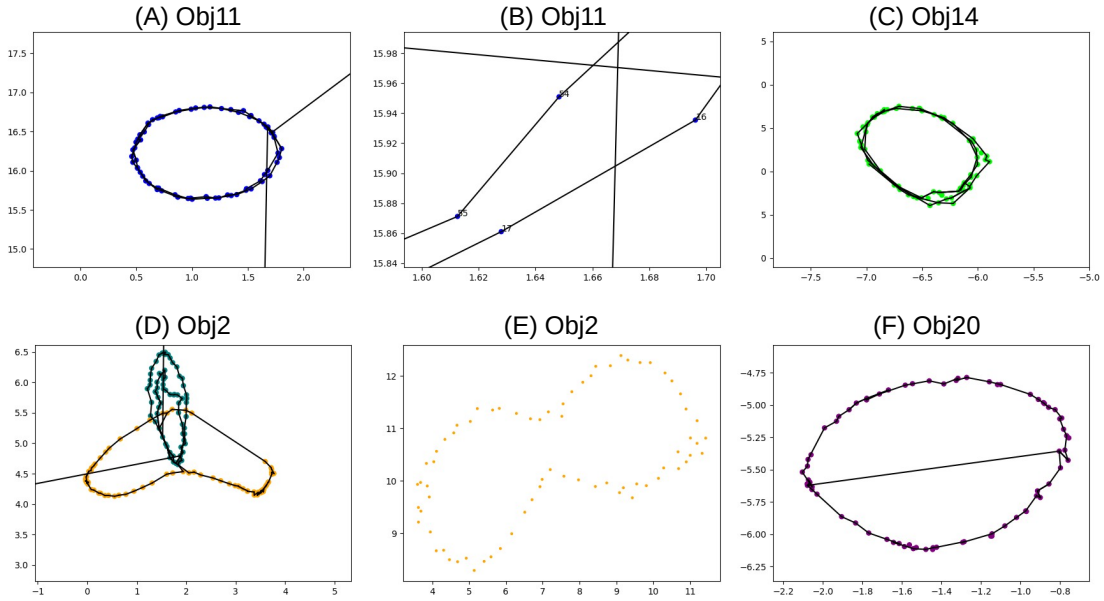


Figure 18: Zoom ins of Figure 16 (D) on the four objects for which our DM-PCD post processed output captures a different loop than the UMAP projection. (A) Object 11 - While it appears at first glance that the DM-PCD output matches the loop the UMAP projection contains, a closer look reveals (B) that the DM-PCD output actually captures two loops. (C) Object 14 - Similarly to Object 11, the DM-PCD output contains multiple loops and UMAP projection only captures one. (D) Object 2 - UMAP projection is not a complete loop, but DM-PCD produces a complete loop. (E) Object 2 - UMAP projection of only Object 2's images - a complete loop is visible. (F) Object 20 - UMAP projection shows a single loop, while the DM-PCD output captures the same loop, but has an additional edge dividing the loop.

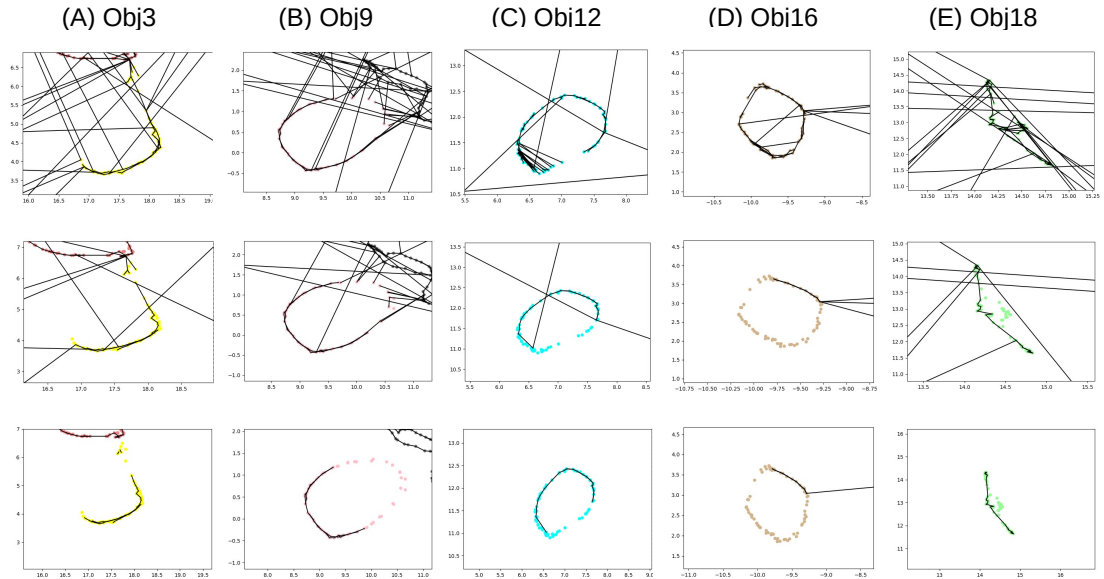


Figure 19: Zoom ins of DM-PCD outputs with persistence thresholds $\delta = 0$ (first row), $\delta = 56$ (second row), and $\delta = 56$ with critical edges longer than 1700 removed (third row). The objects of focus are Object 3(A), Object 9 (B), Object 12 (C), Object 16 (D), and Object 18 (E).

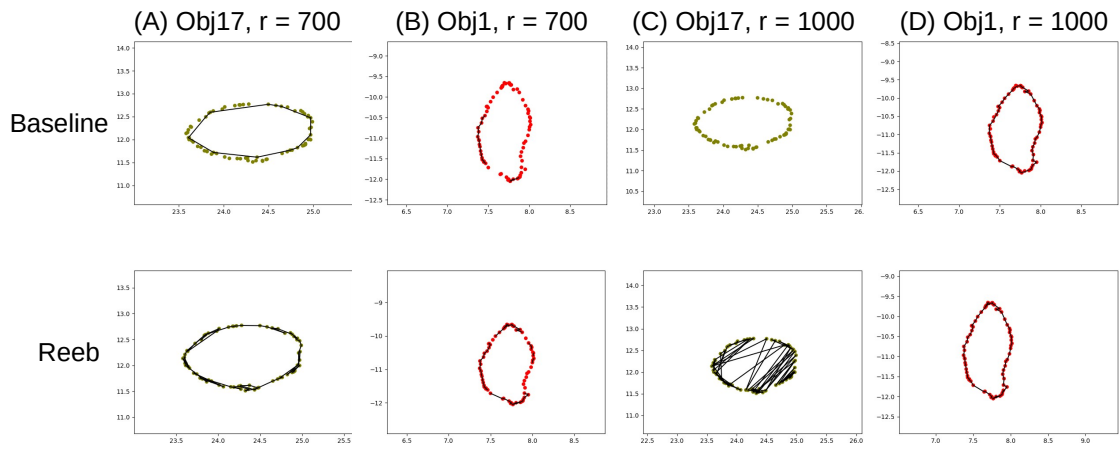


Figure 20: Objects 1 and 17 with baseline and ReebRecon outputs. (A) Object 17, $r = 700$ - Object 17 is captured by both methods. (B) Object 1, $r = 700$ - Object 1 is not captured by either method. (C) Object 17, $r = 1000$ - Object 17 is not captured by either method. (D) Object 1, $r = 1000$ - Object 1 is captured by both methods.